Electronic Supplementary Material (ESI) for Chemical Science.
This journal is © The Royal Society of Chemistry 2023

Supporting Information

Synthesis, bridgehead functionalization, and photoisomerization of 9,10-diboratatriptycene dianions

Sven E. Prey, Jannik Gilmer, Samira V. Teichmann, Luis Čaić, Mischa Wenisch, Michael Bolte, Alexander Virovets, Hans-Wolfram Lerner, Felipe Fantuzzi and Matthias Wagner*

Table of contents:

1. Experimental details and characterization data	ESI1
2. Plots of spectra	ESI15
3. Computational details	ESI32
4. X-ray crystal structure determinations	ESI45
5. References	ESI54

1. Experimental details and characterization data

General considerations. All reactions, manipulations, and analyses were carried out in an argon-filled glovebox or by applying standard Schlenk techniques under an argon atmosphere. Toluene, Et_2O, and THF were dried over Na/benzophenone; C_6D_6, DME, and THF-d_8 were dried over Na-K alloy without benzophenone. CH_2Cl_2 and CD_2Cl_2 were dried over CaH_2. Prior to use, the solvents were distilled from the drying agent, degassed by applying three freeze-pump-thaw cycles, and stored over activated molecular sieves (3 Å).

For photochemical reactions, a medium pressure Hg vapor lamp was used (Heraeus Noblelight; TQ 150, 150 W).

NMR spectra were recorded at 298 K using the following *Bruker* spectrometers: Avance-300, Avance-400, or Avance-500. Chemical shifts are referenced to (residual) solvent signals ($^1H/^{13}C\{^1H\}$: THF-d_8: δ = 3.58/67.21 ppm; CD_2Cl_2: δ = 5.32/53.84 ppm)[S1] or external $BF_3{\cdot}OEt_2$ (^{11}B; $^{11}B\{^1H\}$). Abbreviations: s = singlet, d = doublet, t = triplet, q = quartet, quint = quintet, sext = sextet, m = multiplet, v = virtual, br = broad, $h_{1/2}$ = full width at half maximum, *i* = ipso, *o* = ortho, *m* = meta, *p* = para.

LDI-MS spectra were recorded on a MALDI LTQ Orbitrap XL (*Thermo Fisher Scientific*) in the negative ion mode. The resolution was set to 60000. The sample spots were prepared inside a glovebox: a suspension of a finely powdered sample in Et_2O was transferred to the sample holder by a transfer pipette to form a thin layer of material after evaporation. A desiccator was used to bring the sample holder from the glovebox to the mass spectrometer. In a typical experiment, the laser energy was set to 50 µJ and 20 – 30 spectra were accumulated to increase the signal-to-noise ratio. The isotopic pattern of a selected ion species was compared to the theoretical pattern calculated from the elemental composition of the anion.

Synthesis of K_2[3]

In a glovebox, KC_8 (13 mg, 0.096 mmol) was added in one portion to a solution of **3** (5 mg, 0.012 mmol) in THF (2 mL). The yellow solution immediately adopted a dark green color. After stirring at room temperature for 1 h, the suspension was filtered through a G4 frit and the solid residue was washed with THF (3 x 1 mL). The combined filtrates can be used for further reactions without purification.

X-ray quality crystals of $[K_2(dme)_3]$[**3**] were obtained by slow partial evaporation of a DME solution of K_2[**3**].

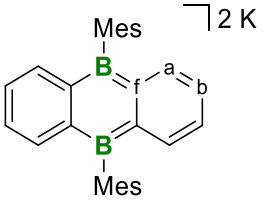

Figure S1. Numbering scheme for K_2[**3**].

*NMR shifts of compound K_2[**3**]*
^{1}H NMR (500.2 MHz, THF-d_8): δ = 7.73 – 7.59 (br, 4H, H-a), 6.87 – 6.77 (br, 4H, Mes-H), 6.45 – 6.33 (br, 4H, H-b), 2.30 (s, 6H, Mes-*p*-CH_3), 2.15 (s, 12H, Mes-*o*-CH_3).

^{11}B NMR (160.5 MHz, THF-d_8): δ = 28.3 ($h_{1/2}$ = 430 Hz).

^{13}C{^{1}H} NMR (125.8 MHz, THF-d_8): δ = 152.4* (Mes-*i*-C), 141.4 (Mes-*o*-C), 138.0 (br, C-f), 136.3 (C-a), 131.9 (Mes-*p*-C), 127.1 (Mes-*m*-C), 115.2 (C-b), 24.9* (Mes-*o*-CH$_3$), 21.3 (Mes-*p*-CH$_3$). *) The positions of these signals were confirmed by crosspeaks in the ^{1}H/^{13}C-HMBC NMR spectrum.

Synthesis of Li[4]

t-BuLi (2.35 M in *n*-pentane, 0.38 mL, 0.89 mmol) was added dropwise to a solution of 1,2-diiodobenzene (0.12 mL, 0.92 mmol) in THF/Et_2O (1:1, 12 mL) at –110 °C. After stirring at –110 °C for 30 min, a solution of **1** (144 mg, 0.71 mmol) in THF (2 mL) was added via syringe. The reaction mixture was allowed to warm to room temperature and stirred overnight. After evaporation to dryness, the remaining colorless solid was washed with *n*-hexane (3 x 1 mL), dried in vacuo, dissolved in C_6H_6 (4 mL) and freeze-dried overnight. The fine powder was dissolved in C_6H_6 (1 mL) and *n*-hexane (6 mL) was added quickly to precipitate a colorless solid. After washing the precipitate with *n*-hexane (2 x 1 mL) and drying in a dynamic vacuum, the product $[Li(thf)_{1.5}]$[**4**] was obtained as colorless powder (76 mg, 21 %).

X-ray quality crystals of $[Li(thf)_2]$[**4**] were obtained from a saturated solution of $[Li(thf)_{1.5}]$[**4**] in C_6H_6/*n*-hexane (1:5).

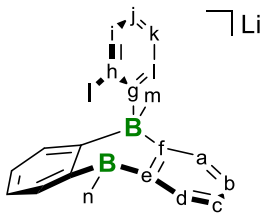

Figure S2. Numbering scheme for Li[**4**].

*NMR shifts of compound Li[**4**]*

^{1}H NMR (500.2 MHz, THF-d_8): δ = 7.93 (dd, ^{3}J(H,H) = 7.3 Hz, ^{4}J(H,H) = 1.2 Hz, 2H, H-d), 7.83 (br d, ^{3}J(H,H) = 7.2 Hz, 1H, H-l), 7.40 (dd, ^{3}J(H,H) = 7.6 Hz, ^{4}J(H,H) = 1.3 Hz, 1H, H-i), 7.12 (vtd, ^{3}J(H,H) = 7.2 Hz, ^{3}J(H,H) = 7.2 Hz, ^{4}J(H,H) = 1.3 Hz, 1H, H-k), 7.01 (br d, ^{3}J(H,H) = 7.3 Hz, 2H, H-a), 6.88 (vtd, ^{3}J(H,H) = 7.3 Hz, ^{3}J(H,H) = 7.3 Hz, ^{4}J(H,H) = 1.2 Hz, 2H, H-b), 6.82 (vtd, ^{3}J(H,H) = 7.3 Hz, ^{3}J(H,H) = 7.3 Hz, ^{4}J(H,H) = 1.5 Hz, 2H, H-c), 6.53 – 6.46 (m, 1H, H-j), 1.29 (s, 3H, H-n), –(0.04–0.07) (m, 3H, H-m).

^{11}B NMR (160.5 MHz, THF-d_8): δ = 63.5 ($h_{1/2}$ = 900 Hz, *B*CH$_3$), –10.1 (Ar*B*CH$_3$).

^{13}C{^{1}H} NMR (125.8 MHz, THF-d_8): δ = 180.5 (q, ^{1}J(C,B) = 50 Hz, C-f), 170.0 (q, ^{1}J(C,B) = 50 Hz, C-g), 145.5 (C-e), 139.4 (C-i), 136.6 (C-l), 134.5 (C-d), 133.1 (C-a), 128.9 (C-b), 125.4 (C-k), 124.5 (C-j), 120.8 (C-c), 111.7 (C-h), 22.9 (q, ^{1}J(C,B) = 38 Hz, C-m), 4.9 (C-n).

Cyclization attempts on [Li(thf)$_{1.5}$][4]

In a glovebox, Mg flakes (50 mg, 2.06 mmol) were added to a solution of [Li(thf)$_{1.5}$][**4**] (30 mg, 0.057 mmol) in THF (2 mL). The reaction was analyzed by ^{1}H NMR spectroscopy daily. 1,2-Dibromoethane (3 µL, 0.0035 mmol) was added to the reaction mixture, because no reaction had taken place over the course of one week. After another 3 d at room temperature, the transformation was complete according to ^{1}H NMR spectroscopy. The turbid solution was filtered through a 0.22 µm RC syringe filter, evaporated, the obtained colorless solid washed with C_6H_6 (0.5 mL), and dried in vacuo. 10 mg of a colorless solid were obtained, that consisted mainly of the 9,10-diboratatriptycene species [**5**]$^{2-}$, as judged by NMR spectroscopy (see Figure S3).

The same reaction was also carried out on a smaller scale in THF-d_8 to obtain high-quality reaction-NMR spectra. For unknown reasons, this reaction took place already in the absence of 1,2-dibromoethane. A plot of the reaction-NMR spectra is shown in Figure S4.

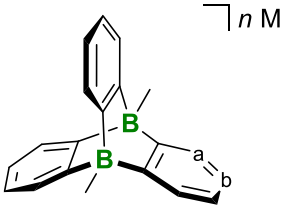

Figure S3. Numbering scheme for M$_n$[**5**] (*n* M = Mg^{2+} or Li^{+} + ½ Mg^{2+}).

*NMR shifts of compound M_n[**5**] (n M = ½ Mg^{2+} or Li^+ + ½ Mg^{2+})*

^{1}H NMR (300.0 MHz, THF-d_8): δ = 7.29 – 7.21 (br, 6H, H-a), 6.52 – 6.35 (m, 6H, H-b), 0.61 – 0.51 (br, 6H, BCH_3).

^{11}B NMR (96.3 MHz, THF-d_8): δ = –13.2.

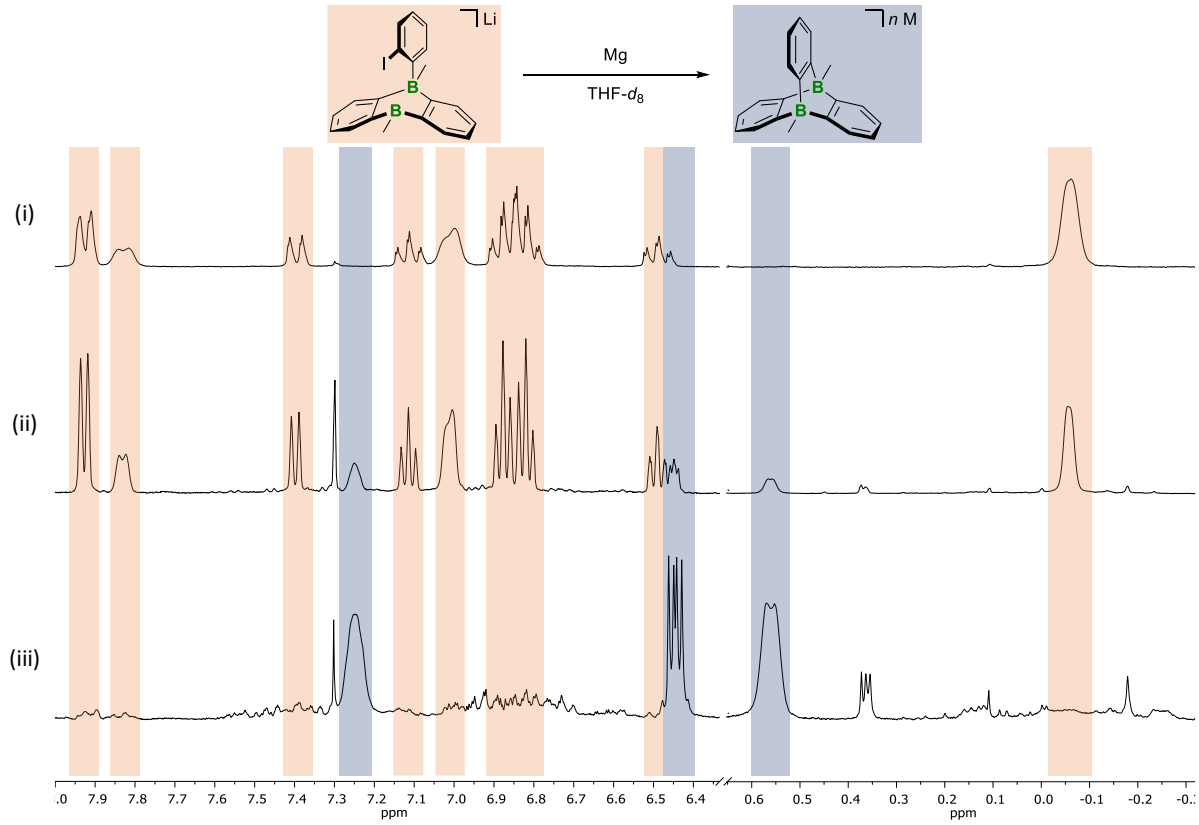

Figure S4. NMR spectra recorded on the reaction mixture of [Li(thf)$_{1.5}$][**4**] and Mg in THF-d_8. (i) 250.1 MHz, THF-d_8, start of the reaction; (ii) 400.1 MHz, THF-d_8, after 2 d at room temperature; (iii) 250.1 MHz, THF-d_8, after 7 d at room temperature. (*n* M = Mg^{2+} or Li^+ + ½ Mg^{2+})

Synthesis of Li_2[5]

A freshly prepared solution of LiN(*i*-Pr)$_2$ (0.71 mmol) in THF (5 mL) was added at –78 °C to a mixture of C_6H_5F (70 µL, 0.75 mmol) and Li_2[**1**], which had been freshly prepared at room temperature from **1** (116 mg, 0.57 mmol) and Li metal (24 mg, 3.46 mmol) in THF (10 mL) according to the literature procedure.[S2] The reaction mixture was slowly allowed to warm to room temperature and stirred overnight. The resulting yellow solution was filtered through a G4 frit and the filtrate was evaporated to dryness. The solid crude product was dissolved in THF (1 mL) and the resulting yellow solution was partially evaporated over a period of several days, until a crystalline colorless precipitate formed. The supernatant was removed, the solid was washed with *n*-hexane (3 x 0.5 mL) and dried in vacuo to give the product as its THF solvate complex [Li(thf)]$_2$[**5**]. The yield of the compound varied between 50–75%.

Note: The compound is formed as THF solvate, which was typically dried in a dynamic vacuum (oil pump; approximately 10^{-3} torr, room temperature, 10 to 20 min). After this drying process, the

number of remaining thf ligands typically varies between individual samples. It is therefore advisable to determine the individual THF content of each sample by means of ^{1}H NMR spectroscopy.

The crystalline material obtained by the above-mentioned slow evaporation of a THF solution of Li_2[**5**] was not suitable for X-ray crystallography.

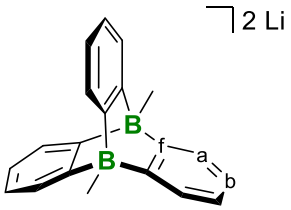

Figure S5. Numbering scheme for Li_2[**5**].

*NMR shifts of compound Li_2[**5**]*
^{1}H{^{11}B} NMR (500.2 MHz, THF-d_8): δ = 7.27 – 7.22 (br m, 6H, H-a), 6.46 – 6.41 (m, 6H, H-b), 0.58 – 0.53 (br m, 6H, BCH_3).

^{11}B NMR (160.5 MHz, THF-d_8): δ = –13.2.

^{13}C{^{1}H} NMR (125.8 MHz, THF-d_8): δ = 170.5 – 169.4 (m, C-f), 126.9 (C-a), 119.9 (C-b), 1.0 – (–0.1) (B*C*H_3).

Synthesis of K_2[6]

A solution of C_6H_5Li (93 mg, 1.11 mmol) in THF (5 mL) was added at –78 °C to a mixture of C_6H_5F (0.15 mL, 1.61 mmol) and K_2[**2**], which had been freshly prepared at room temperature from **2** (150 mg, 0.85 mmol) and KC_8 (460 mg, 3.41 mmol) in THF (10 mL) according to the literature procedure.[S2] The reaction mixture was slowly allowed to warm to room temperature and stirred overnight. The resulting yellow solution was filtered through a G4 frit and the filtrate was evaporated to dryness. The solid crude product was dissolved in 1,2-dimethoxyethane (DME; 3 mL). Gas-phase diffusion of *n*-hexane into the yellow solution at –30 °C for several days led to the precipitation of a colorless crystalline solid. The mother liquor was removed, the solid was washed with *n*-hexane (4 x 2 mL) and dried in vacuo to yield the product as its DME solvate complex [K_2(dme)][**6**] (147 mg, 41%).

Note: The compound is formed as DME solvate, which was typically dried in a dynamic vacuum (oil pump; approximately 10^{-3} torr, room temperature, 10 to 20 min). After this drying process, the number of remaining dme ligands typically varied between individual samples and with respect to the DME content of corresponding single-crystalline material (cf. the X-ray crystal structure analyses). It is therefore advisable to determine the individual DME content of each sample by means of ^{1}H NMR spectroscopy. Sometimes crystallization was retarded. In these cases, the addition of seed crystals from a previous crop led to precipitation of the desired product overnight at –30 °C.

X-ray quality crystals of [K(dme)$_2$][K(dme)][**6**] were obtained by gas-phase diffusion of *n*-hexane into a DME solution of K_2[**6**] at room temperature.

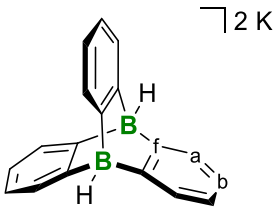

Figure S6. Numbering scheme for K_2[**6**].

*NMR shifts of compound [K_2(dme)$_{0.5}$][**6**]*
^{1}H{^{11}B} NMR (500.2 MHz, THF-d_8): δ = 7.30 – 7.24 (br m, 6H, H-a), 6.53 – 6.47 (m, 6H, H-b), 3.36 (s, 2H, B*H*).

^{11}B NMR (160.5 MHz, THF-d_8): δ = –8.3 (d, ^1J(B,H) = 87 Hz).

^{13}C{^{1}H} NMR (125.8 MHz, THF-d_8): δ = 170.2 – 169.0 (m, C-f), 130.0 (C-a), 120.6 (C-b).

*Mass-spectrometric characterization of K_2[**6**]*
LDI-MS(–): *m/z* = 251.15 ([$C_{18}H_{14}B_2$ - H]$^-$, calcd.: 251.12)

Synthesis of K_2[7]

A solution of C_6H_5Li (26 mg, 0.31 mmol) in THF (4 mL) was added at –78 °C to a mixture of C_6H_5F (0.04 mL, 0.41 mmol) and K_2[**3**], which had been freshly prepared at room temperature from **3** (85 mg, 0.21 mmol) and KC_8 (112 mg, 0.83 mmol) in THF (8 mL) according to the literature procedure.[S3] The reaction mixture was slowly allowed to warm to room temperature and stirred for 5 d. The resulting pale brown solution was filtered through a G4 frit and the filtrate was evaporated to dryness. The solid crude product was dissolved in 1,2-dimethoxyethane (DME; 1 mL) and the solution was partially evaporated over a period of several days, until a crystalline colorless precipitate formed.

X-ray quality crystals of [K(dme)$_2$][K(dme)][**7**] were obtained by slow partial evaporation of a DME solution of K_2[**7**].

Note: Since the reaction does not proceed selectively and furnished only a few crystals of [K(dme)$_2$][K(dme)][**7**], no yield was determined and no NMR spectra of the compound were recorded.

Synthesis of [*n*-Bu_4N]$_2$[6]

[*n*-Bu_4N]Cl (10.9 mg, 0.039 mmol) was added to a solution of [K_2(dme)$_2$][**6**] (10.0 mg, 0.020 mmol) in THF (1 mL). The turbid mixture was stirred for 1 h at room temperature and the newly formed colorless solid was collected on a 0.22 µm RC syringe filter. The solid crude product was washed with THF (1 mL), extracted into CH_2Cl_2 (3 x 0.7 mL), and the colorless extract was quickly evaporated to dryness under reduced pressure. The colorless solid was dried in a dynamic vacuum for 20 min to yield [*n*-Bu_4N]$_2$[**6**] (13.4 mg, 93%).

Note: [*n*-Bu_4N]$_2$[**6**] undergoes a slow B–H/B–Cl-exchange reaction in CH_2Cl_2 and CD_2Cl_2 (see below). It is therefore advisable to perform follow-up reactions with freshly prepared solutions of [*n*-Bu_4N]$_2$[**6**].

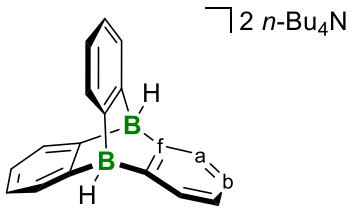

Figure S7. Numbering scheme for [*n*-Bu$_4$N]$_2$[**6**].

*NMR shifts of compound [n-Bu$_4$N]$_2$[**6**]*

^{1}H{^{11}B} NMR (500.2 MHz, CD_2Cl_2): δ = 7.23 – 7.19 (m, 6H, H-a), 6.44 – 6.40 (m, 6H, H-b), 3.25 (s, 2H, B*H*), 2.10 –2.02 (m, 16H, NCH_2), 1.36 –1.26 (m, 16H, NCH$_2$CH_2), 1.09 – 1.01 (m, 16H, NCH$_2$CH$_2$CH_2), 0.99 (t, ^3J(H,H) = 7.3 Hz, 24H, NCH$_2$CH$_2$CH$_2$CH_3).

^{11}B NMR (160.5 MHz, CD_2Cl_2): δ = –7.5 (d, ^1J(B,H) = 82 Hz).

^{13}C{^{1}H} NMR (125.8 MHz, CD_2Cl_2): δ = 171.7 – 170.3 (m, C-f), 129.6 (C-a), 119.5 (C-b), 57.9 (N*C*H$_2$), 24.6 (NCH$_2$*C*H$_2$), 20.0 (NCH$_2$CH$_2$*C*H$_2$), 14.1 (NCH$_2$CH$_2$CH$_2$*C*H$_3$).

*Mass-spectrometric characterization of [n-Bu$_4$N]$_2$[**6**]*

LDI-MS(–): *m/z* = 251.12 ([$C_{18}H_{14}B_2$ - H]$^-$, calcd.: 251.12)

Synthesis of [*n*-Bu$_4$N]$_2$[8]

A freshly prepared solution of [*n*-Bu$_4$N]$_2$[**6**] (0.020 mmol) in CD_2Cl_2 (0.5 mL) was flame-sealed under vacuum and stored at 50 °C overnight. NMR spectra recorded on the reaction mixture revealed that [*n*-Bu$_4$N]$_2$[**6**] had vanished and a new compound, [*n*-Bu$_4$N]$_2$[**8**], had formed along with CD_2HCl and CD_2H_2. The solution was evaporated under reduced pressure and the obtained solid was dried in a dynamic vacuum for 20 minutes to yield [*n*-Bu$_4$N]$_2$[**8**] as colorless solid (14.0 mg, 89%).

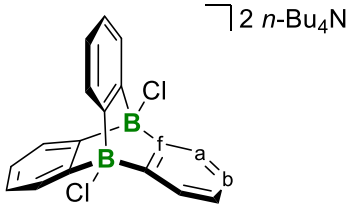

Figure S8. Numbering scheme for [*n*-Bu$_4$N]$_2$[**8**].

*NMR shifts of compound [n-Bu$_4$N]$_2$[**8**]*

^{1}H NMR (500.2 MHz, CD_2Cl_2): δ = 7.51 – 7.47 (m, 6H, H-a or H-b), 6.63 – 6.59 (m, 6H, H-a or H-b), 2.17 – 2.10 (m, 16H, NCH_2), 1.34 – 1.25 (m, 16H, NCH$_2$CH_2), 1.13 – 1.03 (m, 16H, NCH$_2$CH$_2$CH_2), 0.97 (t, ^3J(H,H) = 7.3 Hz, 24H, NCH$_2$CH$_2$CH$_2$CH_3).

^{11}B NMR (160.5 MHz, CD_2Cl_2): δ = 2.4 (br).

^{13}C{^{1}H} NMR (125.8 MHz, CD_2Cl_2): δ = 161.9 (br, C-f), 125.7 (C-a or C-b), 120.9 (C-a or C-b), 57.9 (N*C*H$_2$), 24.6 (NCH$_2$*C*H$_2$), 20.0 (NCH$_2$CH$_2$*C*H$_2$), 14.1 (NCH$_2$CH$_2$CH$_2$*C*H$_3$).

*Mass-spectrometric characterization of [n-Bu$_4$N]$_2$[**8**]*

LDI-MS(–): *m/z* = 285.11 ([$C_{18}H_{12}B_2Cl_2$ - Cl]$^-$, calcd.: 285.08)

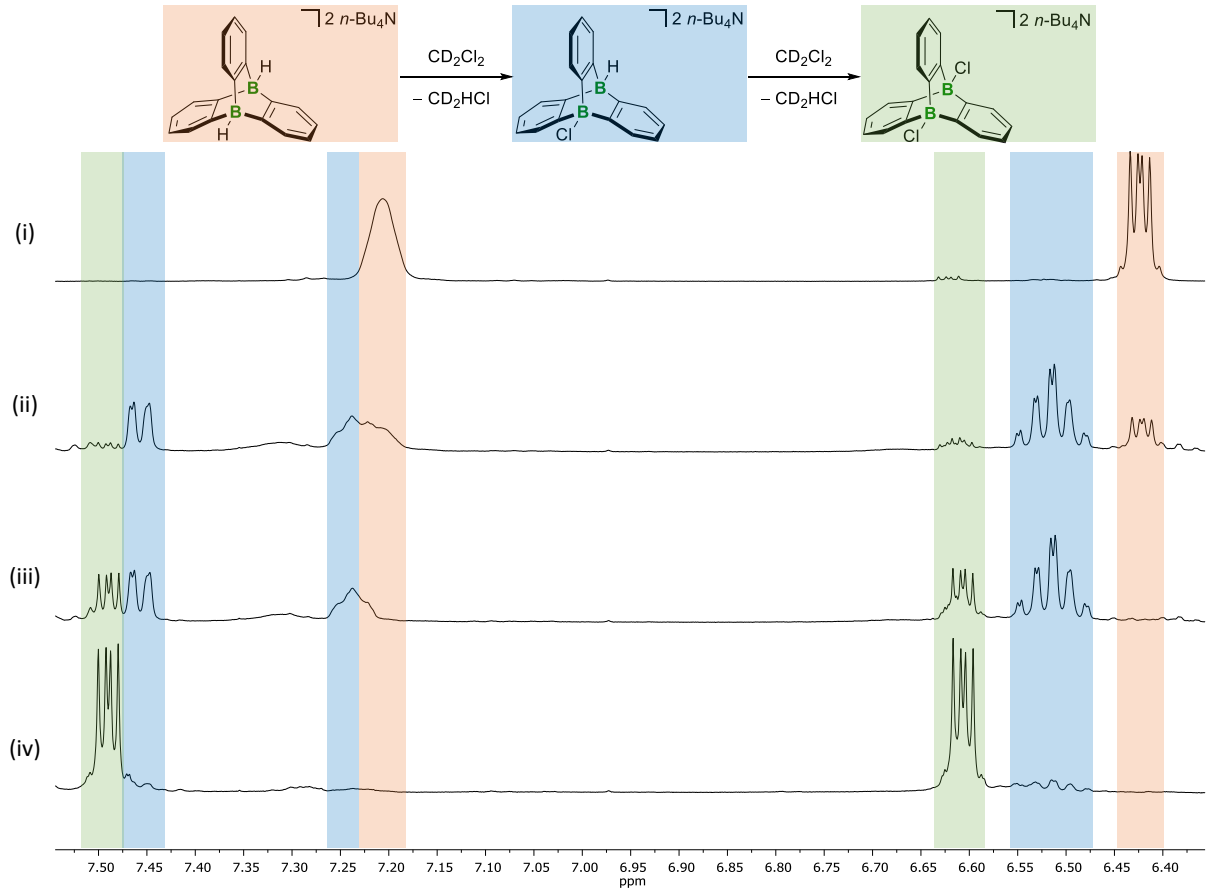

Figure S9. ^{1}H NMR spectra (400.3 MHz, CD_2Cl_2) recorded on a sample of [*n*-Bu_4N]$_2$[**6**] (i) directly after flame-sealing; (ii) after storing it for 19 h at room temperature; (iii) after storing it for 3 d at room temperature and (iv) after storing it for 2 weeks at room temperature. The compound is slowly transformed to its B–Cl derivative [*n*-Bu_4N]$_2$[**8**] likely by sequential B–H/B–Cl exchange.

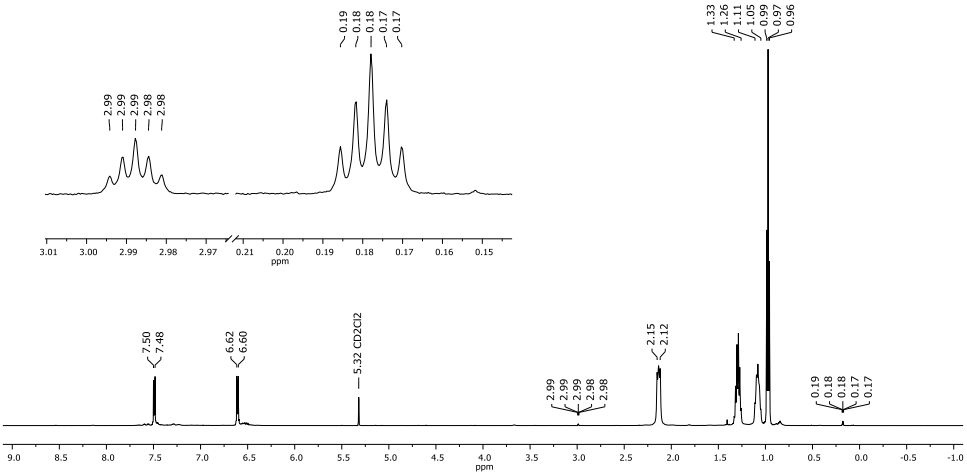

Figure S10. ^{1}H NMR spectrum (500.2 MHz, CD_2Cl_2) recorded on the reaction mixture of the chlorination reaction of [*n*-Bu_4N]$_2$[**6**]. In the close-up picture, the signals of newly formed CD_2HCl (quint. at δ = 2.99 ppm) and CD_2H_2 (quint. at δ = 0.18 ppm) are shown.[S4]

Hydride abstraction experiments on [*n*-Bu$_4$N]$_2$[6]

(i) with $B(C_6F_5)_3$

$B(C_6F_5)_3$ (12.2 mg, 0.024 mmol) in CD_2Cl_2 (0.5 mL) was added to freshly prepared solid [*n*-Bu$_4$N]$_2$[**6**] (0.012 mmol). The resulting clear solution turned turbid within seconds. The suspension was transferred to an NMR tube and flame-sealed under vacuum. In the NMR spectra, only resonances attributable to [*n*-Bu$_4$N][$HB(C_6F_5)_3$] were observed.[S5]

NMR shifts of [n-Bu$_4$N][$HB(C_6F_5)_3$]

^{1}H{^{11}B} NMR (400.3 MHz, CD_2Cl_2): δ = 3.57 (br s, 1H, B*H*), 3.10 – 3.01 (m, 8H, NCH_2), 1.64 – 1.54 (m, 8H, NCH_2CH_2), 1.38 (vsext, ^3J(H,H) = 7.3 Hz, ^3J(H,H) = 7.3 Hz, 8H, $NCH_2CH_2CH_2$), 0.99 (t, ^3J(H,H) = 7.3 Hz, 12H, $NCH_2CH_2CH_2CH_3$).

^{11}B NMR (128.4 MHz, CD_2Cl_2): δ = –25.4 (d, ^1J(B,H) = 92 Hz).

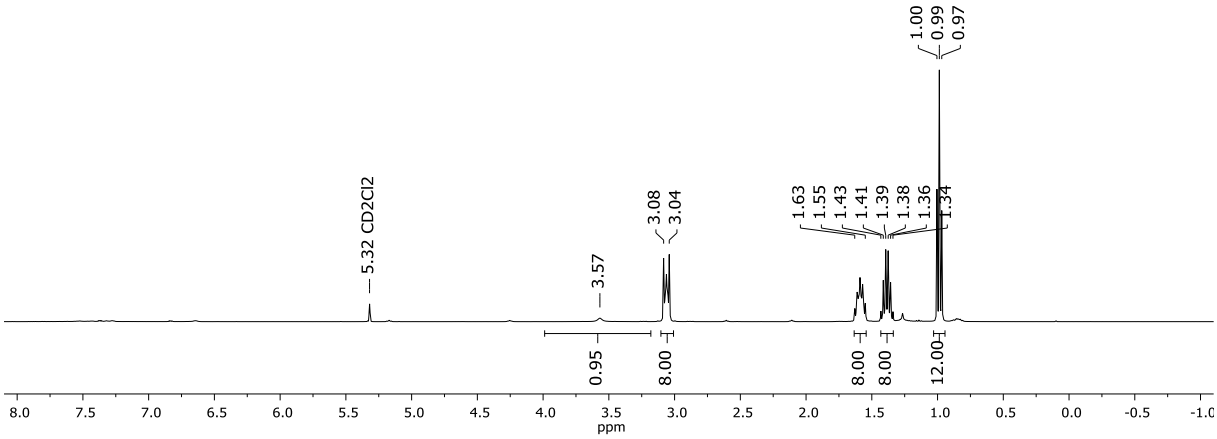

Figure S11. ^{1}H{^{11}B} NMR spectrum (400.3 MHz, CD_2Cl_2) recorded on the mixture of [*n*-Bu$_4$N]$_2$[**6**] and 2 equiv. of $B(C_6F_5)_3$.

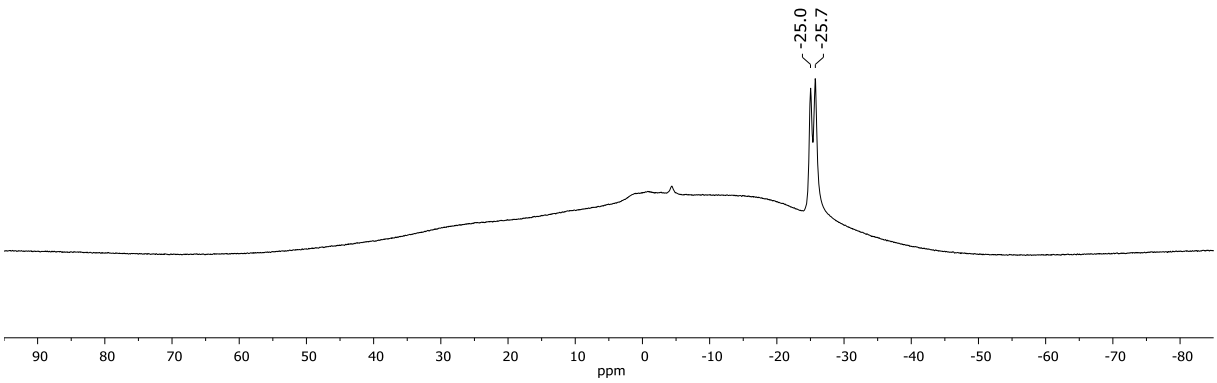

Figure S12. ^{11}B NMR spectrum (128.4 MHz, CD_2Cl_2) recorded on the mixture of [*n*-Bu$_4$N]$_2$[**6**] and 2 equiv. of $B(C_6F_5)_3$.

(ii) with $[Ph_3C][B(C_6F_5)_4]$

A solution of $[Ph_3C][B(C_6F_5)_4]$ (54.0 mg, 0.059 mmol) in CD_2Cl_2 (0.3 mL) was added dropwise to a solution of [*n*-Bu$_4$N]$_2$[**6**] (0.029 mmol) in CD_2Cl_2 (0.3 mL). The turbid green solution was transferred to an NMR tube and flame-sealed under vacuum. In the NMR spectra, only resonances attributable to Ph_3CH and [*n*-Bu$_4$N][$B(C_6F_5)_4$] were observed.

NMR shifts of Ph_3CH

^{1}H NMR (400.3 MHz, CD_2Cl_2): δ = 7.32 – 7.28 (m, 6H), 7.25 – 7.20 (m, 3H), 7.18 – 7.11 (m, 6H), 5.56 (s, 1H).

NMR shifts of [n-Bu$_4$N][B(C$_6$F$_5$)$_4$]

^{1}H NMR (400.3 MHz, CD_2Cl_2): δ = 3.10 – 3.00 (m, 8H, NCH_2), 1.65 – 1.54 (m, 8H, NCH$_2$CH_2), 1.40 (vsext, ^3J(H,H) = 7.3 Hz, ^3J(H,H) = 7.3 Hz, 8H, NCH$_2$CH$_2$CH_2), 1.00 (t, ^3J(H,H) = 7.3 Hz, 12H, NCH$_2$CH$_2$CH$_2$CH_3).

^{11}B NMR (128.4 MHz, CD_2Cl_2): δ = –16.6.

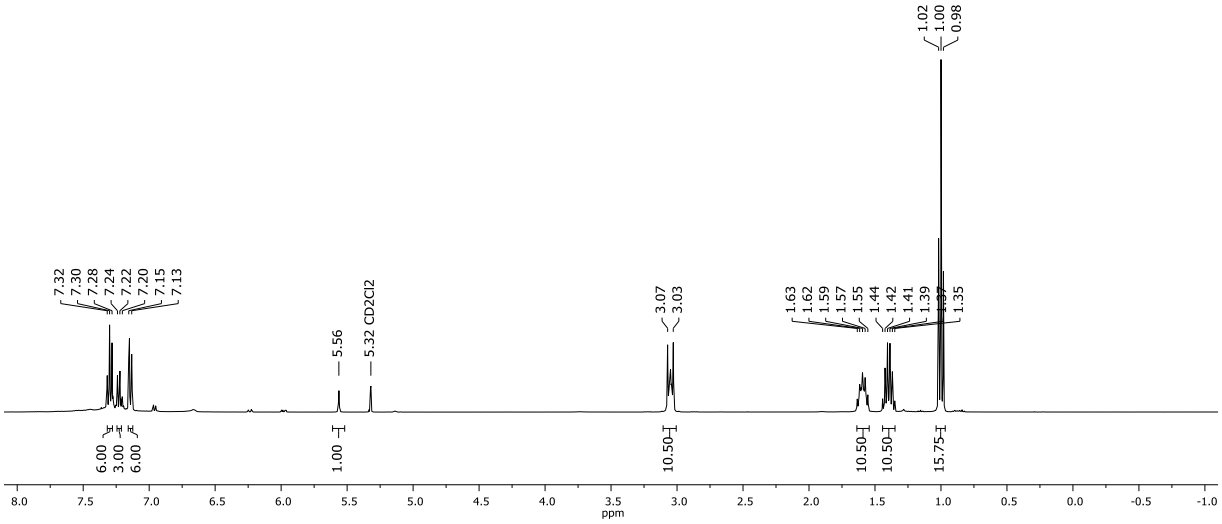

Figure S13. ^{1}H{^{11}B} NMR spectrum (400.3 MHz, CD_2Cl_2) recorded on the mixture of [*n*-Bu$_4$N]$_2$[**6**] and 2 equiv. of [Ph$_3$C][B(C$_6$F$_5$)$_4$]. Note that resonances of [*n*-Bu$_4$N]$^+$ integrate slightly too high, which we attribute to different relaxation behavior of C(sp^2)–H vs. C(sp^3)–H.

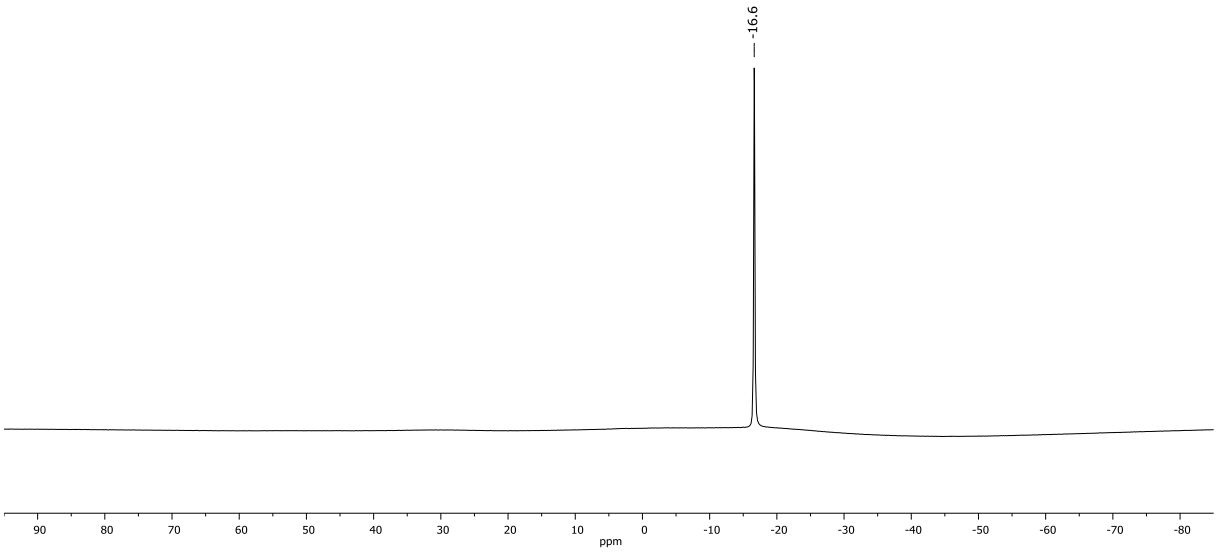

Figure S14. ^{11}B NMR spectrum (128.4 MHz, CD_2Cl_2) recorded on the mixture of [*n*-Bu$_4$N]$_2$[**6**] and 2 equiv. of [Ph$_3$C][B(C$_6$F$_5$)$_4$].

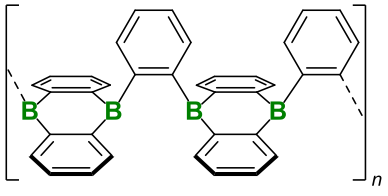

Figure S15. Plausible, but entirely speculative, structure of the precipitate obtained by H$^-$ abstraction from [*n*-Bu$_4$N]$_2$[**6**] with 2 equiv. B(C$_6$F$_5$)$_3$ or [Ph$_3$C][B(C$_6$F$_5$)$_4$].

Synthesis of 9

A mixture of $B(C_6F_5)_3$ (24.4 mg, 0.048 mmol) and SMe_2 (3.5 µL, 0.048 mmol) in CD_2Cl_2 (0.5 mL) was added to freshly prepared solid [*n*-$Bu_4N]_2$[**6**] (0.024 mmol). The resulting clear, colorless solution was transferred to an NMR tube and flame-sealed under vacuum. In the NMR spectra, the selective formation of **9** and [*n*-Bu_4N][$HB(C_6F_5)_3$] was observed.

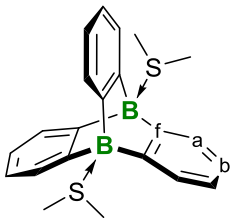

Figure S16. Numbering scheme for **9**.

*NMR shifts of **9***
^{1}H NMR (500.0 MHz, CD_2Cl_2): δ = 7.27 – 7.18 (m, 6H, H-a), 6.91 – 6.85 (m, 6H, H-b), 3.07 (s, 12H, S*C*H_3).

^{11}B NMR (160.5 MHz, CD_2Cl_2): δ = –1.4 ($h_{1/2}$ = 280 Hz).

^{13}C{^{1}H} NMR (125.8 MHz, CD_2Cl_2): δ = 154.5 (br, C-f), 126.2 (C-a), 122.7 (C-b), 21.1 (S*C*H_3).

X-ray quality crystals of **9**·CH_2Cl_2 were obtained directly from the reaction mixture (solvent: CH_2Cl_2) after storage at room temperature for several days.

Photoisomerization of [K_2(dme)][6] – Synthesis of K_2[10]

A colorless solution of [K_2(dme)][**6**] (10.0 mg, 0.024 mmol) in THF (5 mL) was placed in a quartz vessel. The vessel was irradiated with a Hg medium pressure lamp for 1 h. The resulting yellow solution was evaporated to dryness, the yellow solid was re-dissolved in THF-d_8 (0.5 mL) and the solution was transferred to an NMR tube.

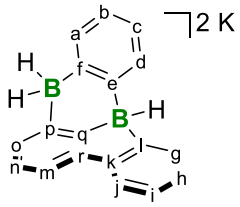

Figure S17. Numbering scheme of K_2[**10**].

*NMR shifts of K_2[**10**]*
^{1}H{^{11}B} NMR (500.2 MHz, THF-d_8): δ = 7.92 – 7.87 (m, 1H, H-g), 7.69 (d, ^3J(H,H) = 7.0 Hz, 1H, H-a), 7.53 – 7.50 (m, 1H, H-j), 7.40 (d, ^3J(H,H) = 7.0 Hz, 1H, H-d), 7.22 (d, ^3J(H,H) = 7.2 Hz, 1H, H-m), 7.15 (d, ^3J(H,H) = 7.2 Hz, 1H, H-o), 6.96 – 6.91 (m, 2H, H-h and H-i), 6.86 (vt, ^3J(H,H) = 7.2 Hz, ^3J(H,H) = 7.2 Hz, 1H, H-n), 6.71 (vt, ^3J(H,H) = 7.0 Hz, ^3J(H,H) = 7.0 Hz, 1H, H-b), 6.65 (vt, ^3J(H,H) = 7.0 Hz, ^3J(H,H) = 7.0 Hz, 1H, H-c), 2.65 (br s, 1H, B*H*), 2.52 (br d, ^2J(H,H) = 14.5 Hz, 1H, *H*BH), 2.40 (br d, ^2J(H,H) = 14.5 Hz, 1H, HB*H*).

^{11}B NMR (160.5 MHz, THF-d_8): δ = –13.7 (d, ^1J(B,H) = 73 Hz, *B*H), –16.7 (vt, ^1J(B,H) = ^1J(B,H) = 78 Hz, H*B*H).

^{13}C{^{1}H} NMR (125.8 MHz, THF-d_8): δ = 173.0* (C-q), 167.9* (C-l), 165.5*(C-e), 161.7* (C-f and C-p), 151.1 (C-k), 144.3 (C-r), 134.4 (C-d), 132.7 (C-g), 130.6 (C-a), 130.1 (C-o), 123.8 (C-n), 123.8 (C-h), 123.0 (C-i), 122.4 (C-b), 122.1 (C-c), 118.9 (C-j), 114.3 (C-m). *) These signals were detected in the ^{1}H/^{13}C-HMBC NMR experiment.

*Mass-spectrometric characterization of K_2[**10**]*
LDI-MS(–): *m/z* = 251.12 ([$C_{18}H_{14}B_2$ - H]$^-$, calcd.: 251.12)

Comparison of the photoisomerizations of K_2[6] and 6^C

In order to compare the photoisomerizations of K_2[**6**] and its all-carbon congener **6^C**, we conducted an additional experiment with identical reaction setups for both species: Solutions of K_2[**6**] and **6^C** (0.039 mmol each) in THF-d_8 (1.5 mL each) were irradiated (Hg medium pressure lamp) in quartz vessels. Samples (0.5 mL each) were taken from the reaction solutions after 20, 40, and 60 min; the samples were transferred to NMR tubes and ^{1}H NMR spectra were recorded (see Figures S18 and S19 below). NMR spectroscopy showed that (i) the isomerization proceeded significantly faster for K_2[**6**] and (ii) the reaction stops at different stages, depending on the bridgehead atom E (E = B: K_2[**10**], E = C: **Int2^C** (cf. Figure 3b)). Note that the higher concentration of K_2[**6**] in the current experiment (0.026 mmol mL^{-1}) led to a significantly slower isomerization reaction compared to the reaction protocol outlined above (0.005 mmol mL^{-1}).

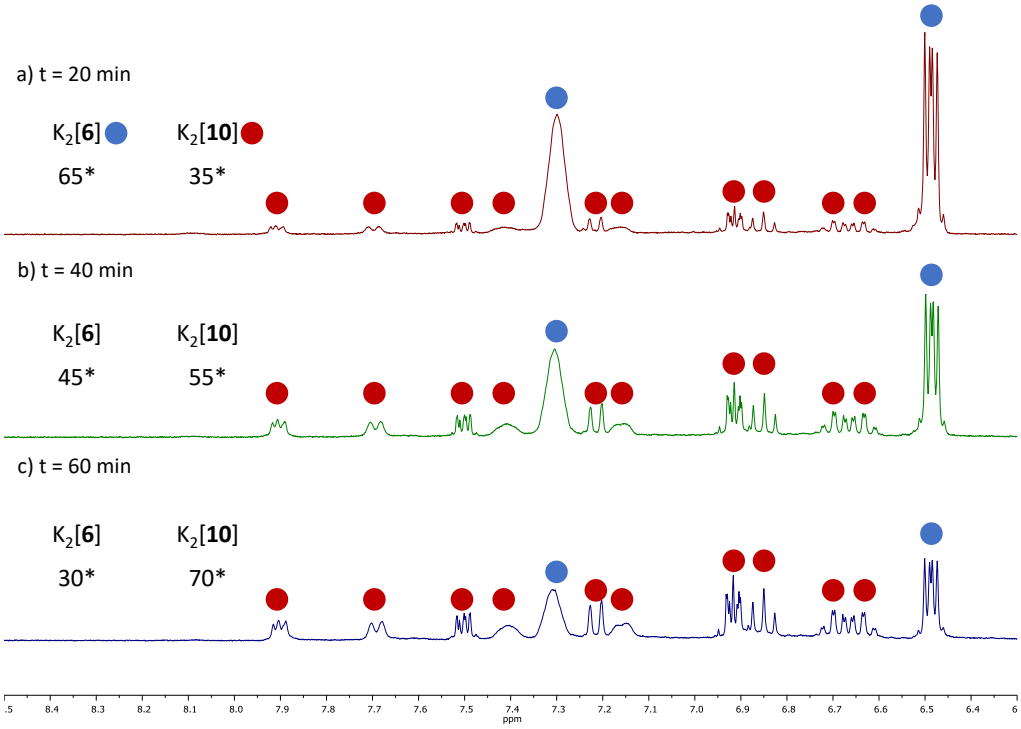

Figure S18. Aromatic regions of the ^{1}H NMR spectra (300.0 MHz, THF-d_8) recorded on the reaction solutions of the photoisomerization reaction of K_2[**6**] after a) 20 min irradiation, b) 40 min irradiation, and c) 60 min irradiation (Hg medium pressure lamp). *) Approximate relative ratios of the starting material K_2[**6**] and the photoproduct K_2[**10**] obtained by integrating the proton signals.

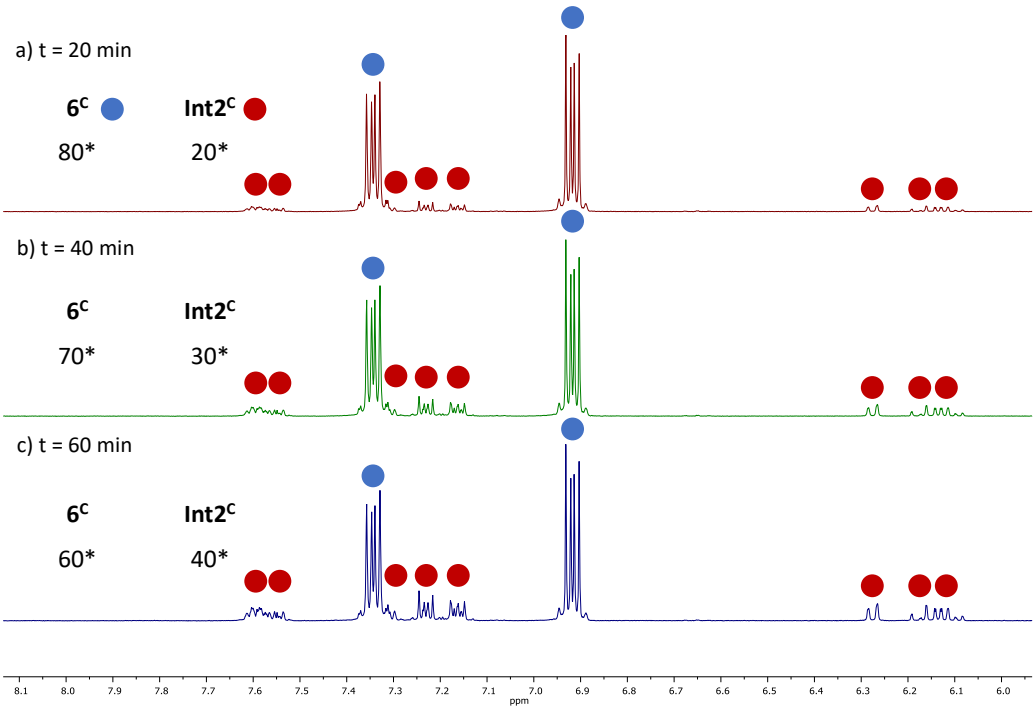

Figure S19. Aromatic regions of the ^{1}H NMR spectra (300.0 MHz, THF-d_8) recorded on the reaction solutions of the photoisomerization reaction of **6^{C}** after a) 20 min irradiation, b) 40 min irradiation, and c) 60 min irradiation (Hg medium pressure lamp). *) Approximate relative ratios of the starting material **6^{C}** and the photoproduct **Int2^{C}** obtained by integrating the proton signals.

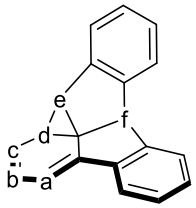

Figure S20. Numbering scheme of **Int2^{C}**.

*NMR shifts of **Int2^{C}***

^{1}H NMR (500.2 MHz, THF-d_8): δ = 7.61 – 7.57 (m, 2H, CH_{aryl}), 7.56 – 7.52 (m, 1H, CH_{aryl}), 7.32 – 7.30 (m, 1H, CH_{aryl}), 7.24 – 7.21 (m, 2H, CH_{aryl}), 7.18 – 7.14 (m, 2H, CH_{aryl}), 6.27 (d, ^{3}J(H,H) = 6.0 Hz, 1H, H-a), 6.16 (dd, ^{3}J(H,H) = 9.4 Hz, ^{3}J(H,H) = 6.0 Hz, 1H, H-b), 6.11 (dd, ^{3}J(H,H) = 9.4 Hz, ^{3}J(H,H) = 4.5 Hz, 1H, H-c), 4.57 (s, 1H, H-f), 2.53 (dd, ^{3}J(H,H) = 4.5 Hz, ^{3}J(H,H) = 2.3 Hz, 1H, H-d), 1.27 (br, 1H, H-e).

The ^{1}H NMR resonances of **Int2^{C}** reported here compare well with those reported in the literature, although the latter had been recorded in CS_2.[S6]

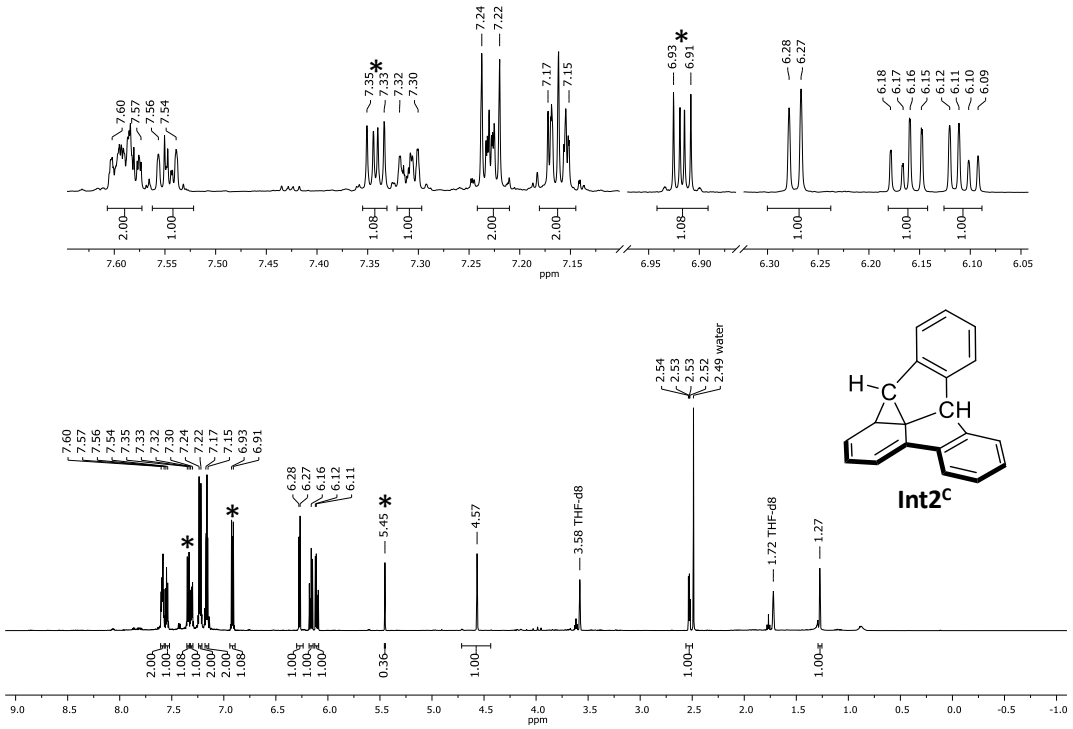

Figure S21. ^{1}H NMR spectrum (500.2 MHz, THF-d_8) recorded on a sample of **6^{C}** after irradiation in a quartz vessel for 4 h to give **Int2^{C}** (cf. Figure 3b; Hg medium pressure lamp). Signals marked with * correspond to unconsumed starting material.

2. Plots of spectra

2.1 Plots of NMR spectra

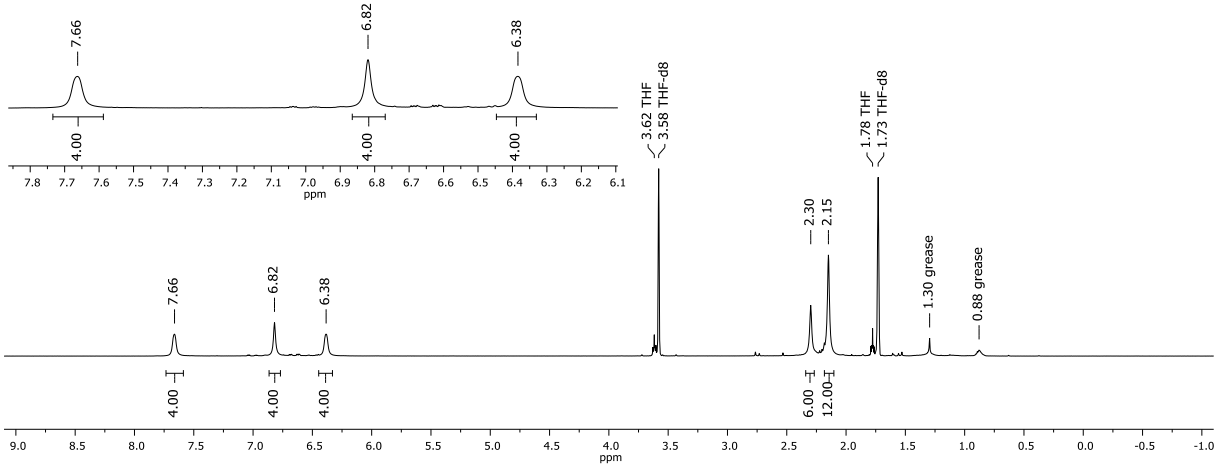

Figure S22. ^{1}H NMR spectrum (500.2 MHz, THF-d_8) of K_2[**3**].

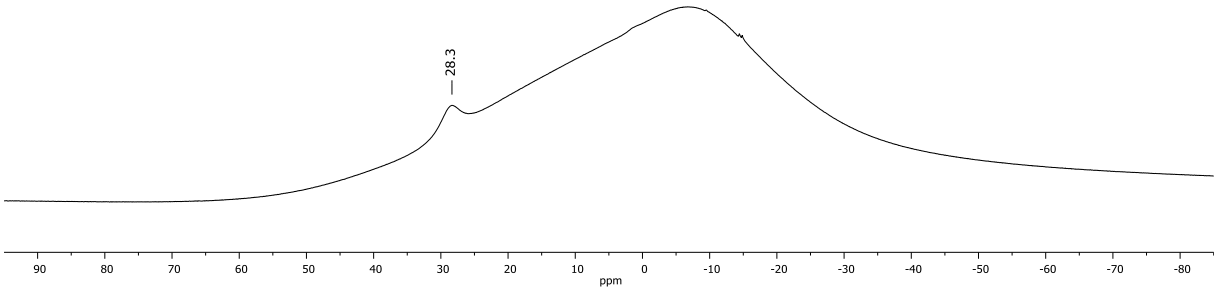

Figure S23. ^{11}B NMR spectrum (160.5 MHz, THF-d_8) of K_2[**3**].

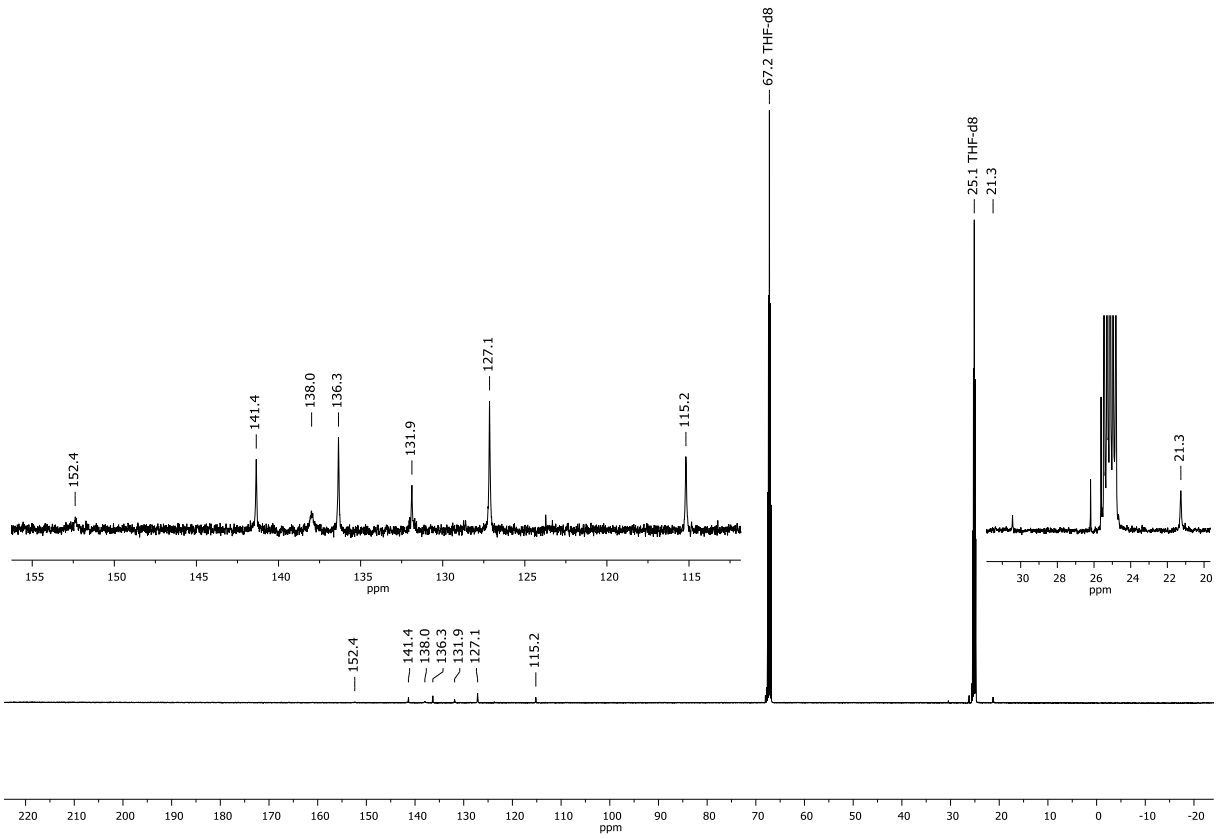

Figure S24. $^{13}C\{^{1}H\}$ NMR spectrum (125.8 MHz, THF-d_8) of K_2[**3**].

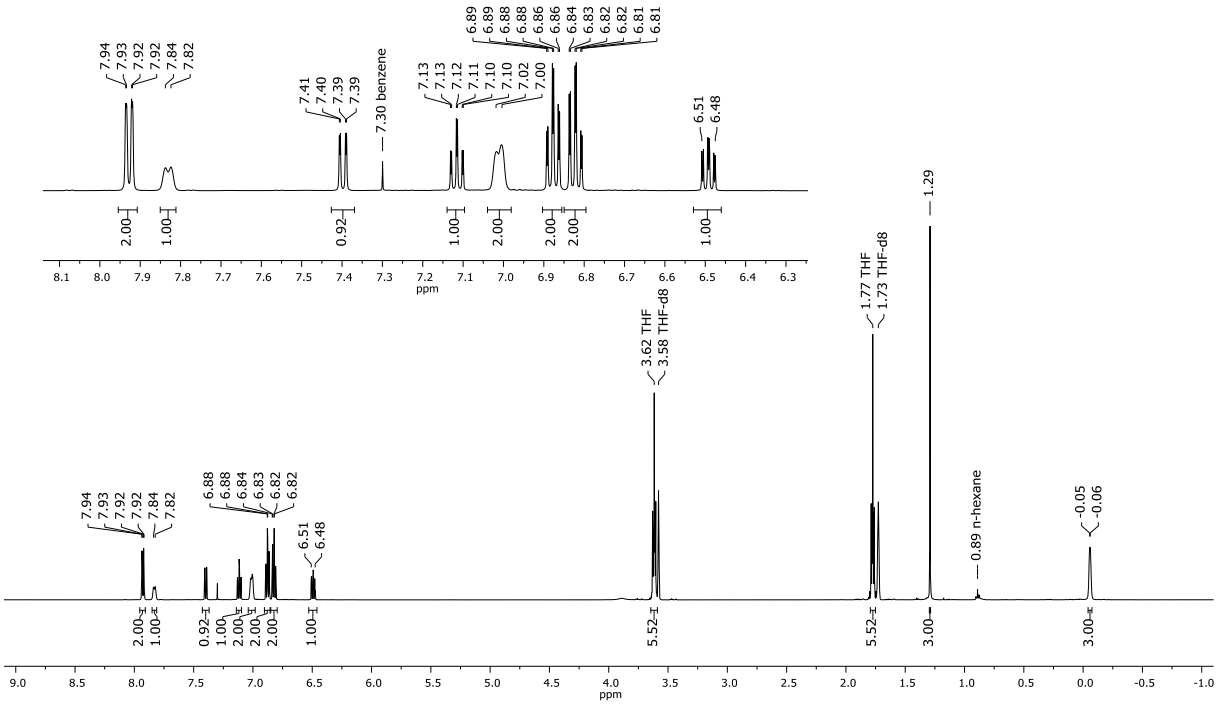

Figure S25. ^{1}H NMR spectrum (500.2 MHz, THF-d_8) of $[Li(thf)_{1.5}]$[**4**].

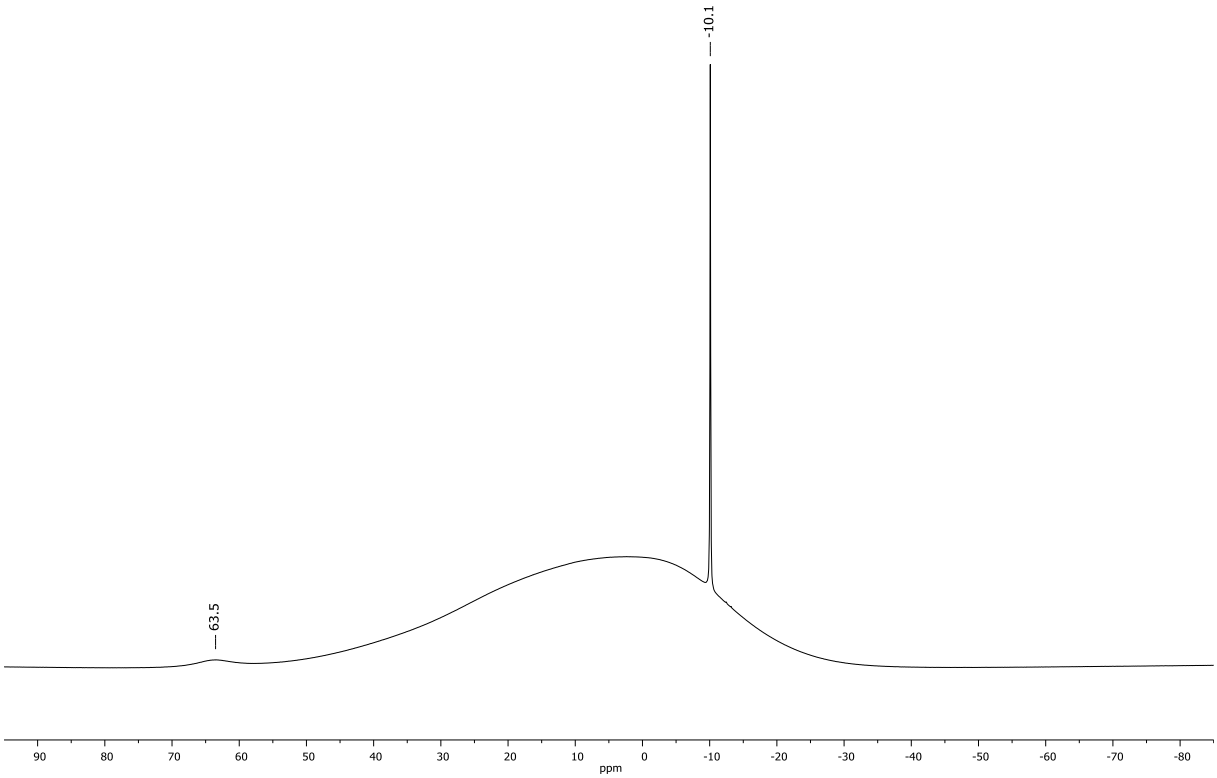

Figure S26. ^{11}B NMR spectrum (160.5 MHz, THF-d_8) of [Li(thf)$_{1.5}$][**4**].

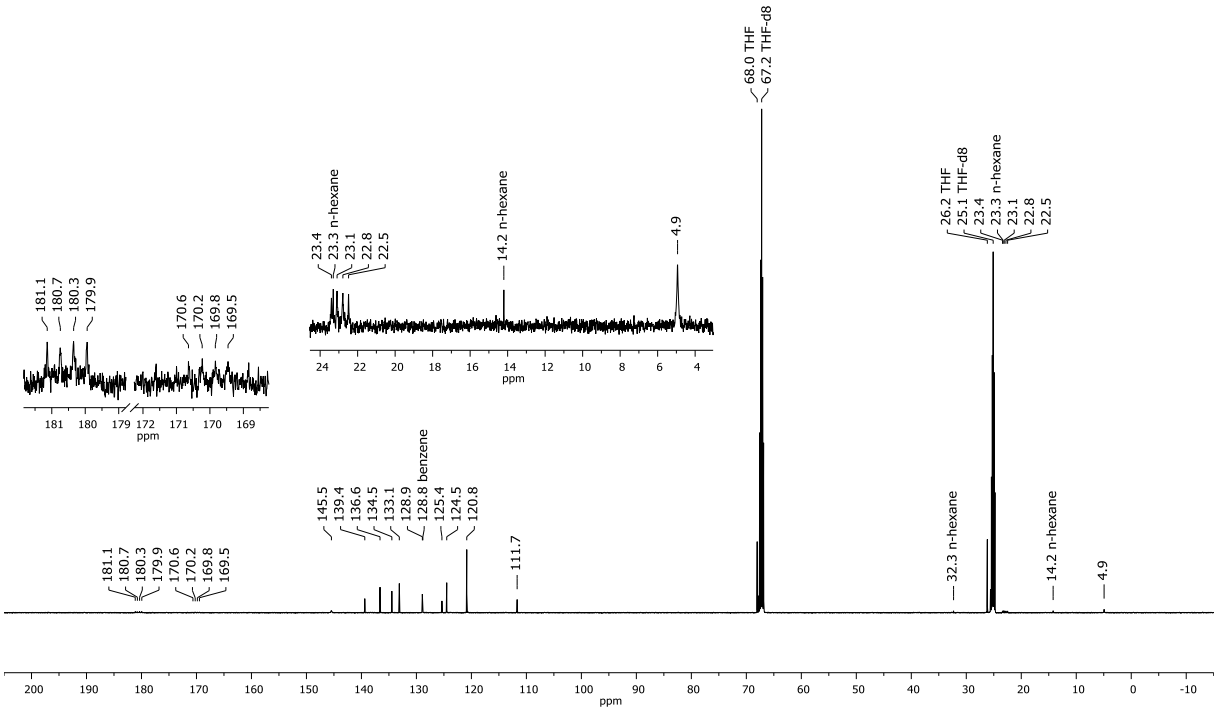

Figure S27. $^{13}C\{^1H\}$ NMR spectrum (125.8 MHz, THF-d_8) of [Li(thf)$_{1.5}$][**4**].

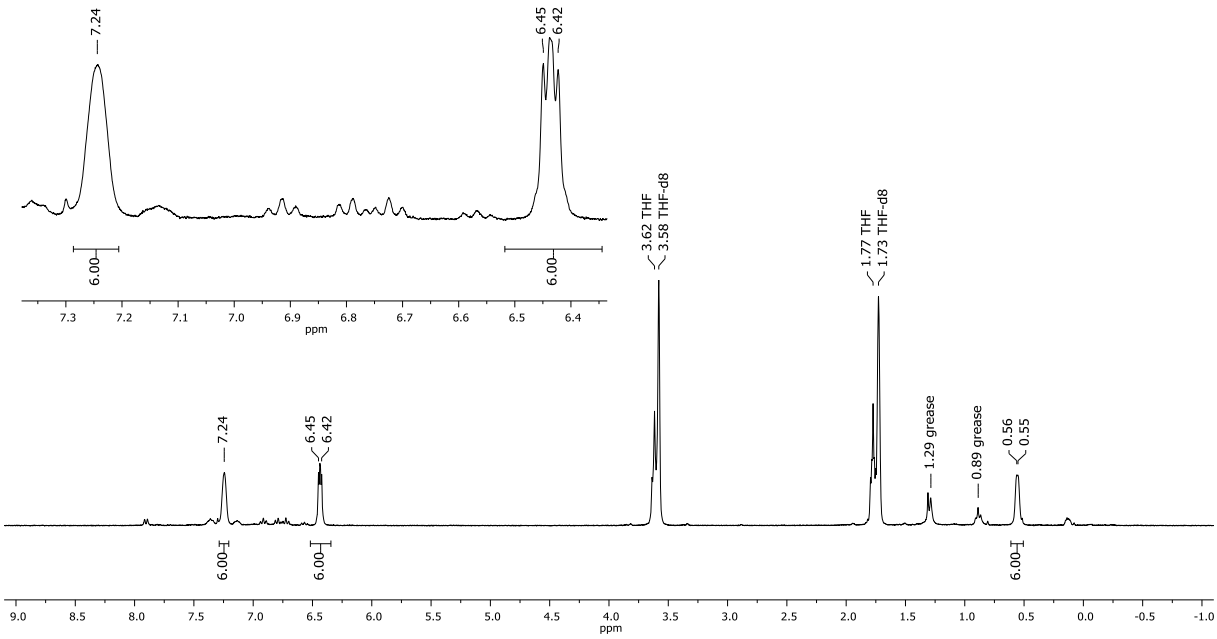

Figure S28. ^{1}H NMR spectrum (300.0 MHz, THF-d_8) of M$_n$[**5**] (*n* M = Mg^{2+} or Li^{+} + ½ Mg^{2+}).

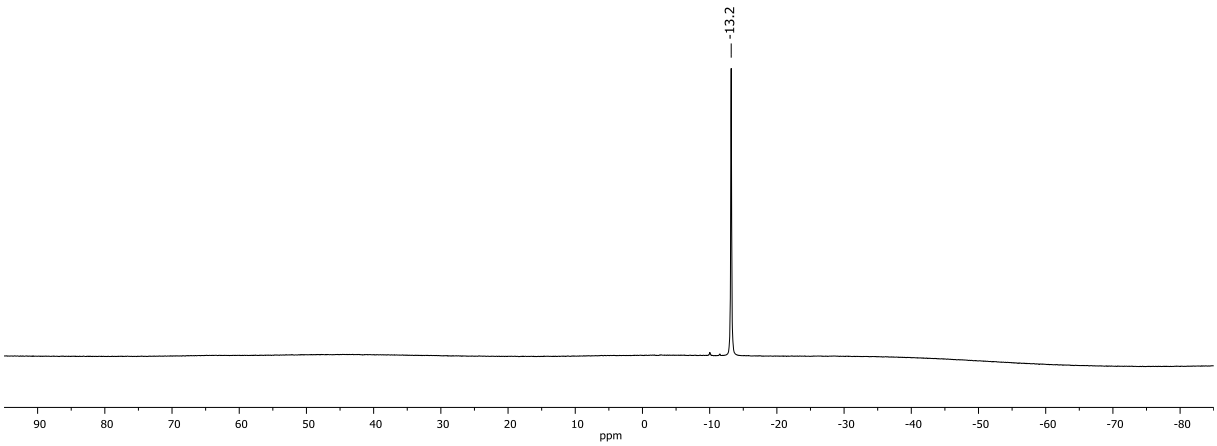

Figure S29. ^{11}B NMR spectrum (96.3 MHz, THF-d_8) of M$_n$[**5**] (*n* M = Mg^{2+} or Li^{+} + ½ Mg^{2+}).

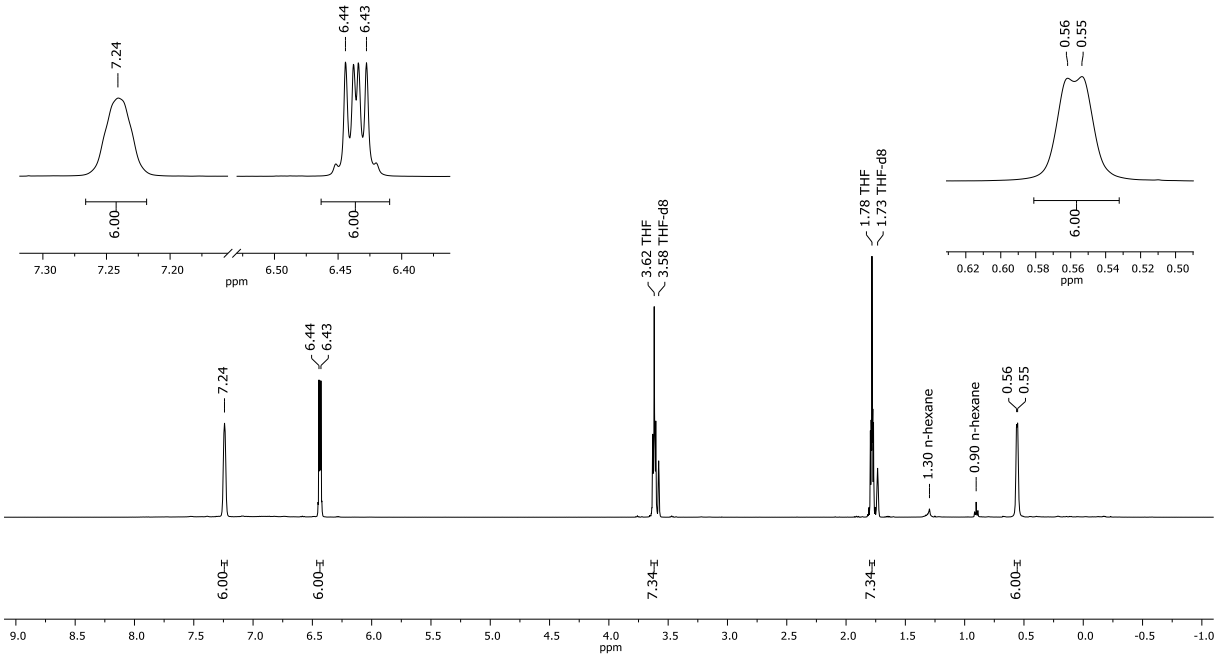

Figure S30. ^{1}H NMR spectrum (500.2 MHz, THF-d_8) of [Li(thf)]$_2$[**5**].

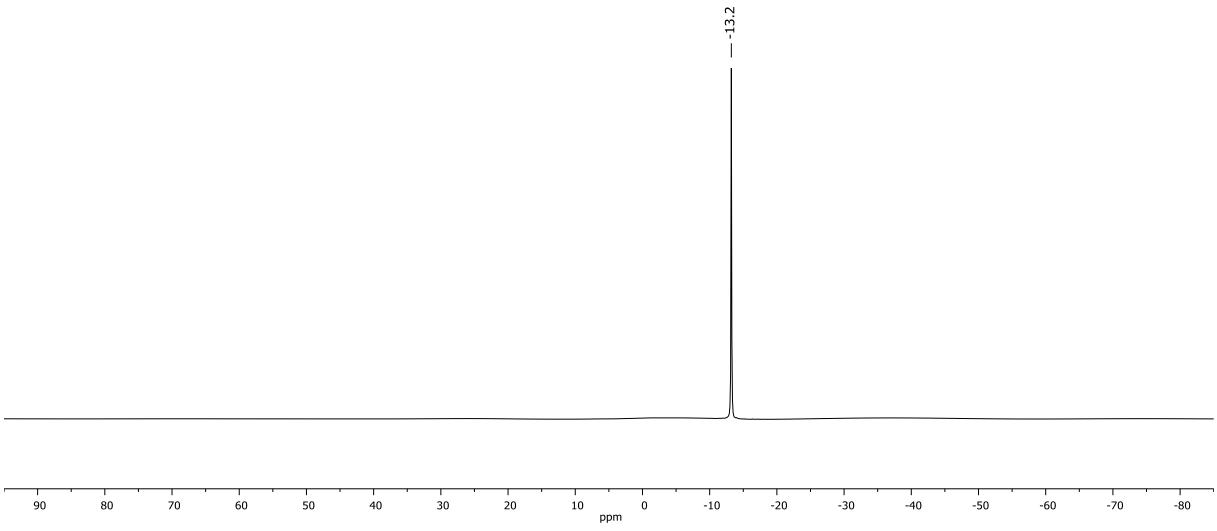

Figure S31. ^{11}B NMR spectrum (160.5 MHz, THF-d_8) of [Li(thf)]$_2$[**5**].

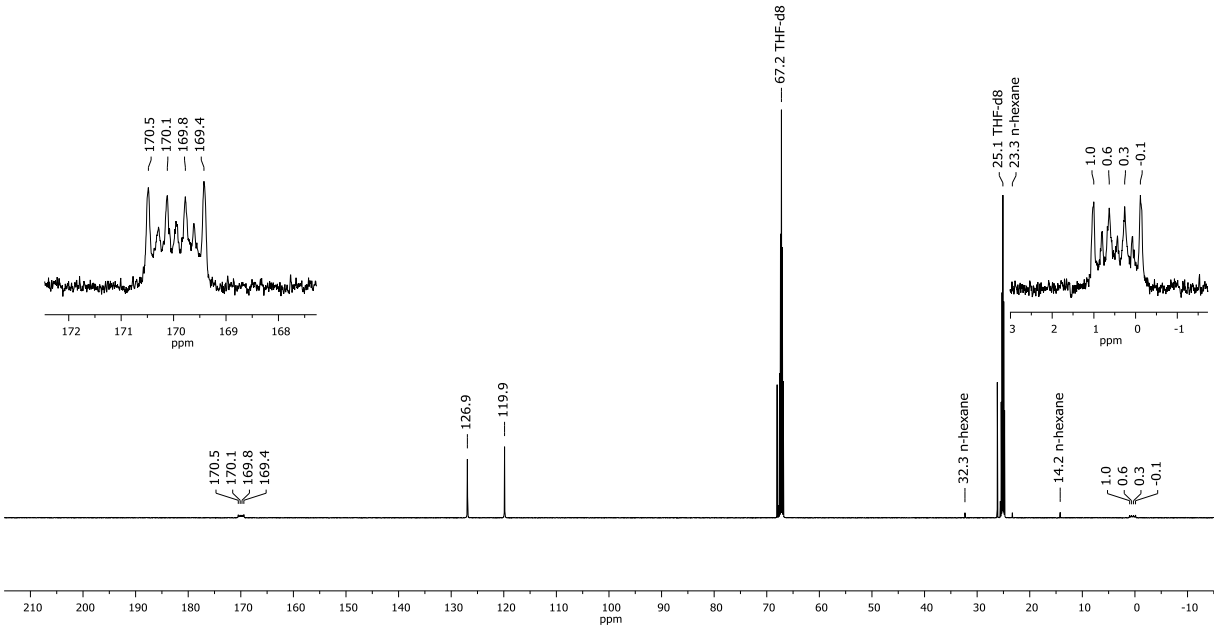

Figure S32. $^{13}C\{^{1}H\}$ NMR spectrum (125.8 MHz, THF-d_8) of $[Li(thf)]_2$[**5**].

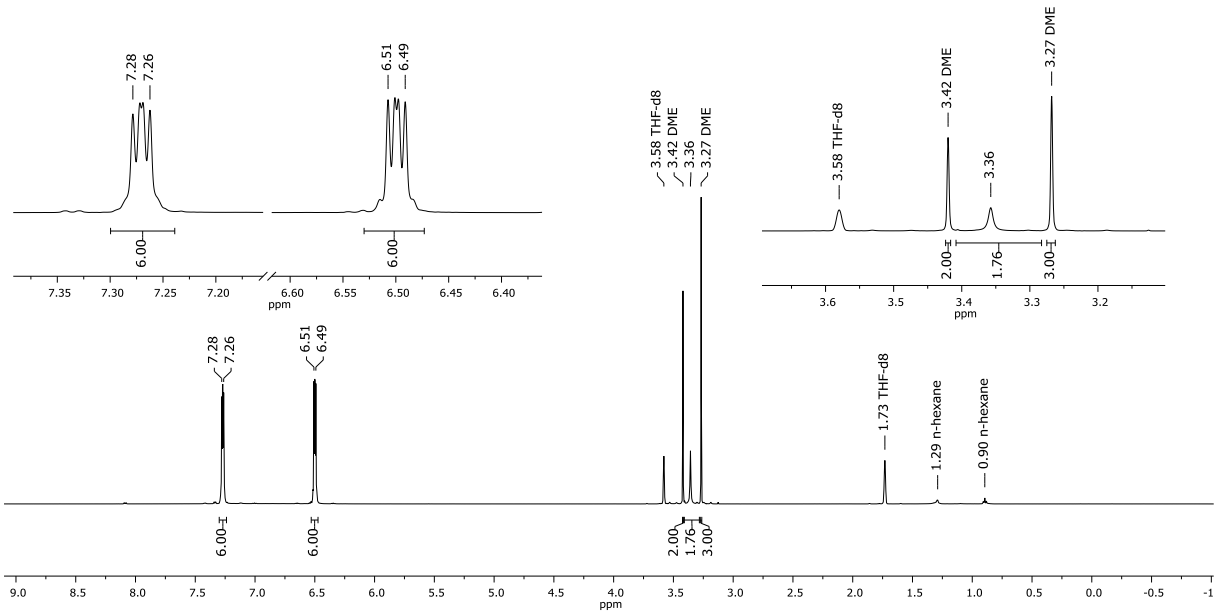

Figure S33. $^{1}H\{^{11}B\}$ NMR spectrum (500.2 MHz, THF-d_8) of $[K_2(dme)_{0.5}]$[**6**].

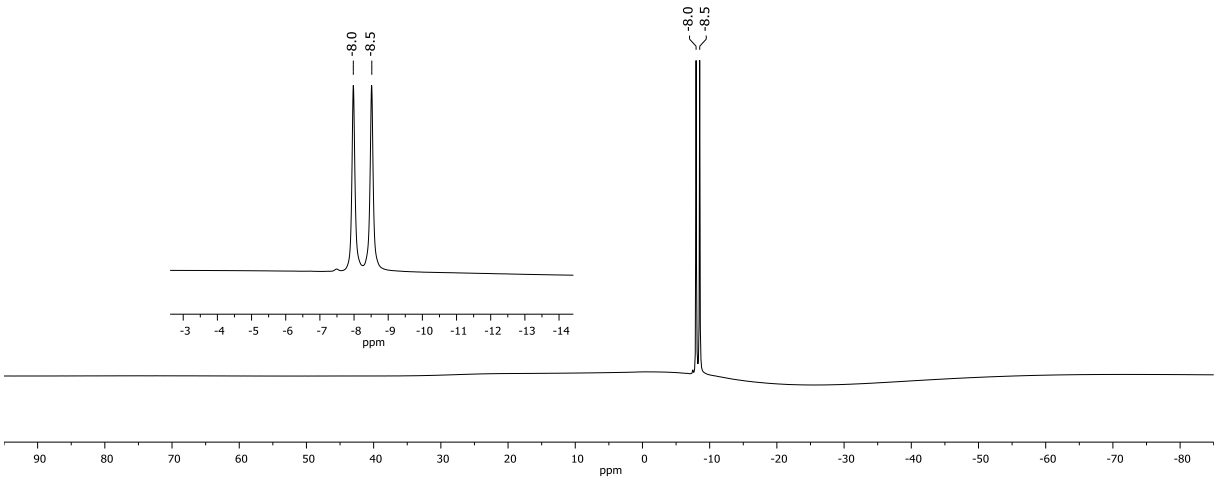

Figure S34. ^{11}B NMR spectrum (160.5 MHz, THF-d_8) of $[K_2(dme)_{0.5}]$[**6**].

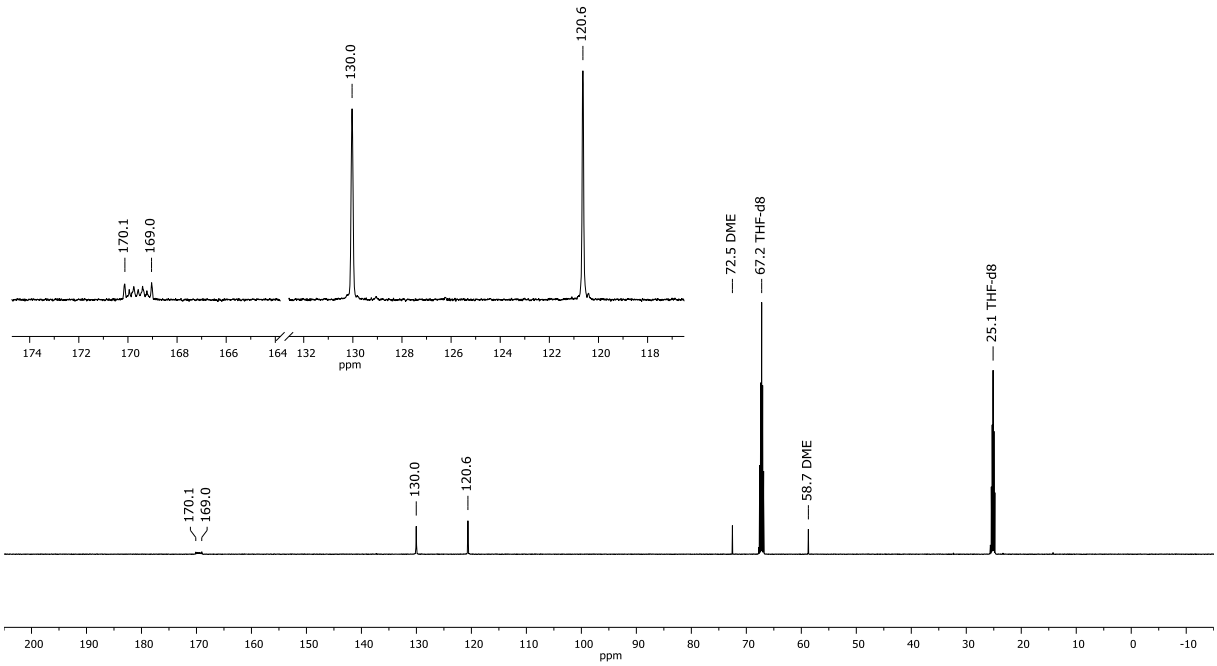

Figure S35. $^{13}C\{^1H\}$ NMR spectrum (125.8 MHz, THF-d_8) of $[K_2(dme)_{0.5}]$[**6**].

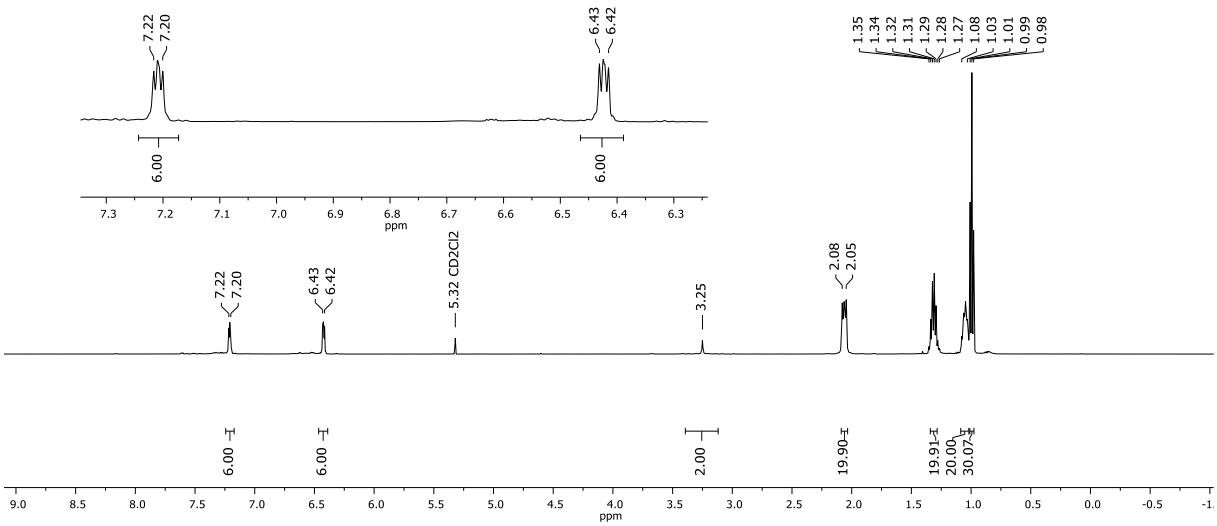

Figure S36. $^{1}H\{^{11}B\}$ NMR spectrum (500.2 MHz, CD_2Cl_2) of $[n\text{-}Bu_4N]_2$[**6**]. Note that resonances of $[n\text{-}Bu_4N]^+$ integrate slightly too high, which we attribute to different relaxation behavior of $C(sp^2)$–H vs. $C(sp^3)$–H.

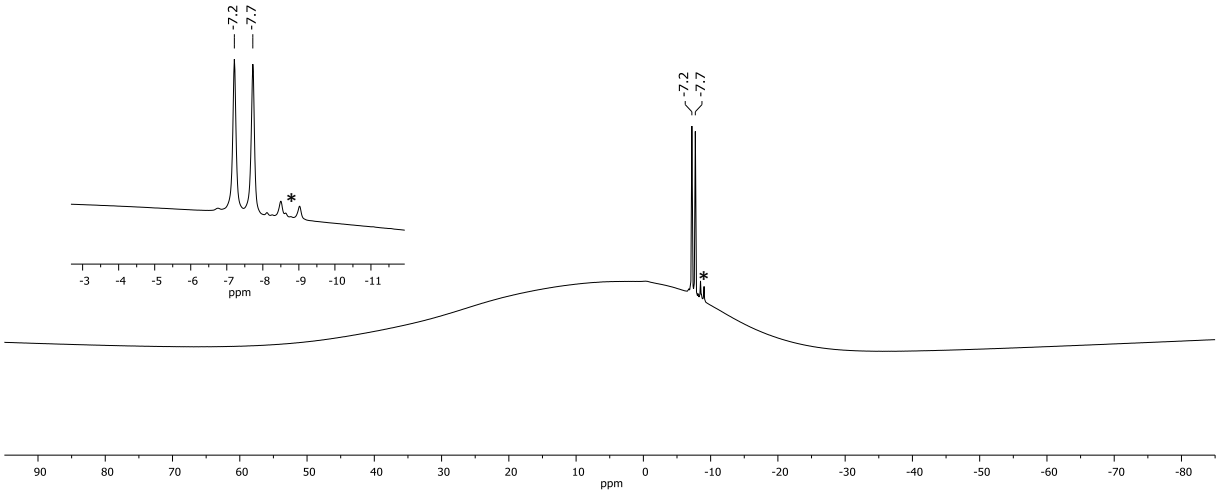

Figure S37. ^{11}B NMR spectrum (160.5 MHz, CD_2Cl_2) of $[n\text{-}Bu_4N]_2$[**6**]. The resonance marked with (*) corresponds to the product of a beginning chlorination of $[\mathbf{6}]^{2-}$ by the solvent.

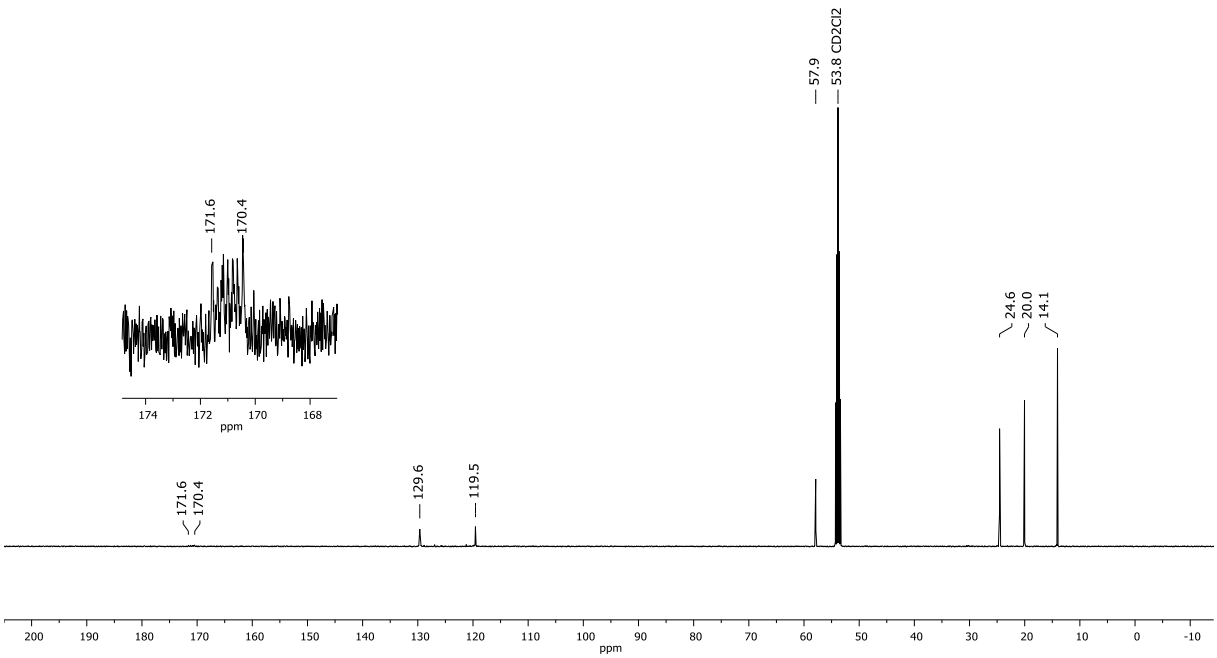

Figure S38. $^{13}C\{^{1}H\}$ NMR spectrum (125.8 MHz, CD_2Cl_2) of $[n\text{-}Bu_4N]_2$[**6**].

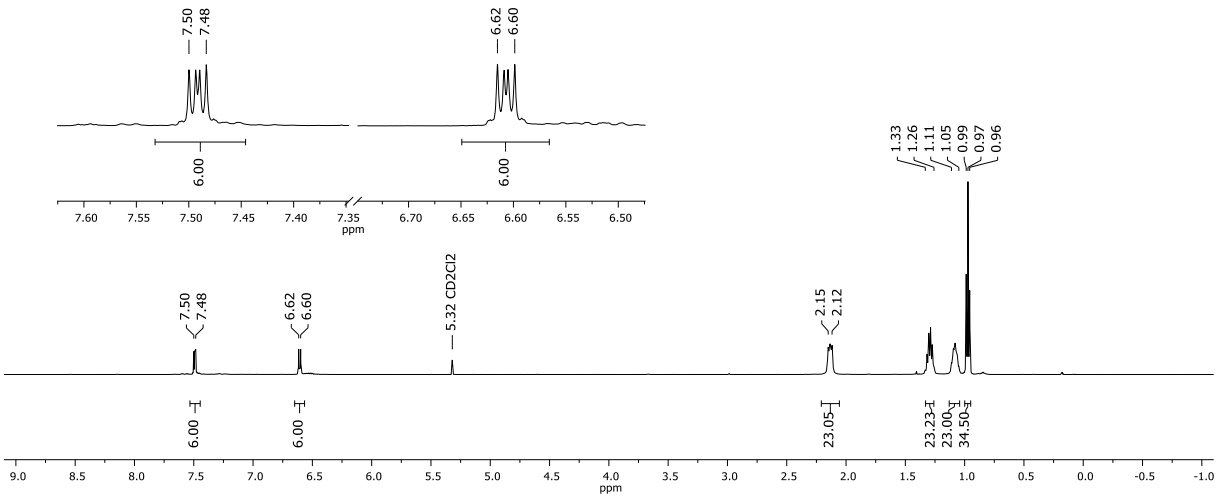

Figure S39. ^{1}H NMR spectrum (500.2 MHz, CD_2Cl_2) of $[n\text{-}Bu_4N]_2$[**8**]. Note that resonances of $[n\text{-}Bu_4N]^+$ integrate slightly too high, which we attribute to different relaxation behavior of $C(sp^2)$–H vs. $C(sp^3)$–H.

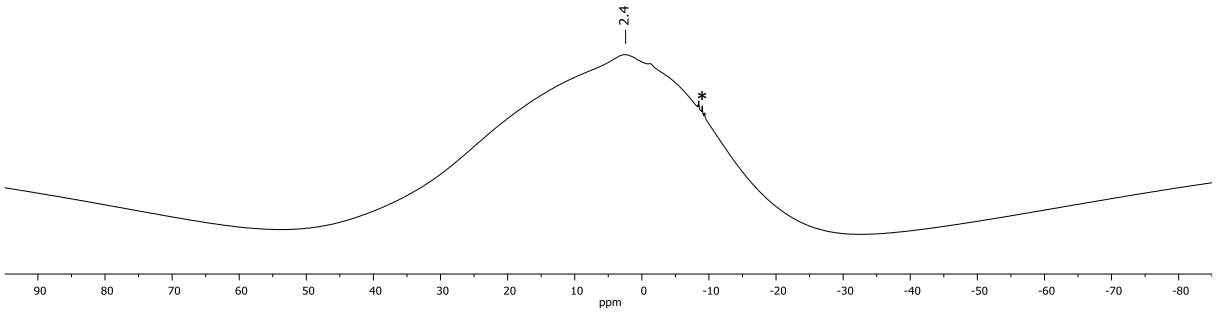

Figure S40. ^{11}B NMR spectrum (160.5 MHz, CD_2Cl_2) of [*n*-Bu_4N]$_2$[**8**]. The resonance marked with (*) corresponds to not fully chlorinated starting material.

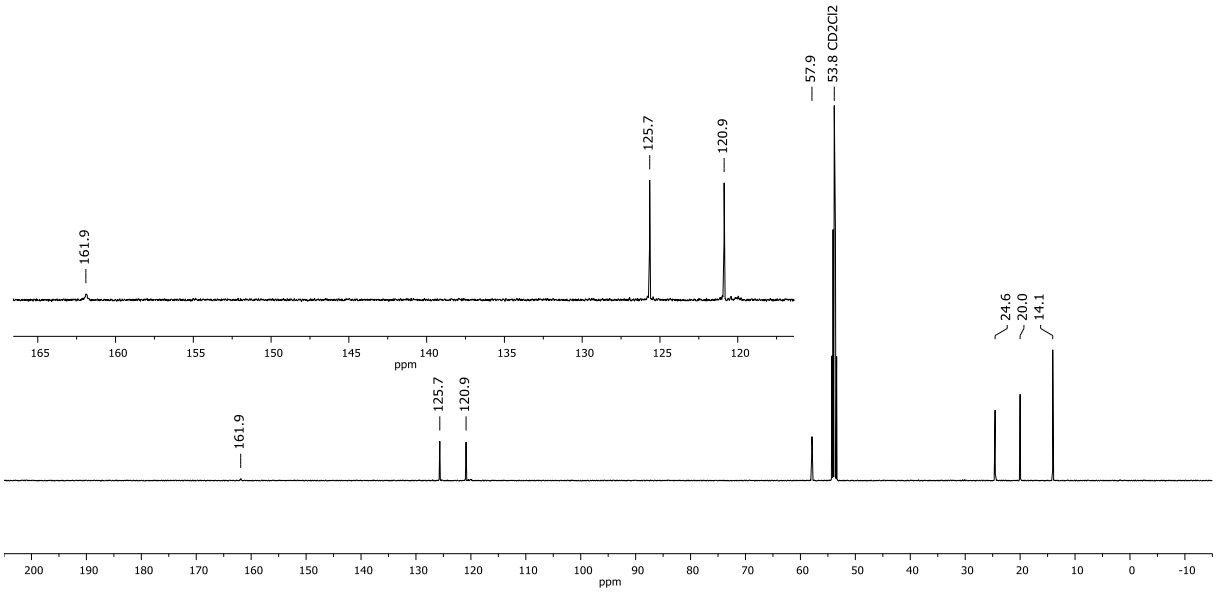

Figure S41. $^{13}C\{^1H\}$ NMR spectrum (125.8 MHz, CD_2Cl_2) of [*n*-Bu_4N]$_2$[**8**].

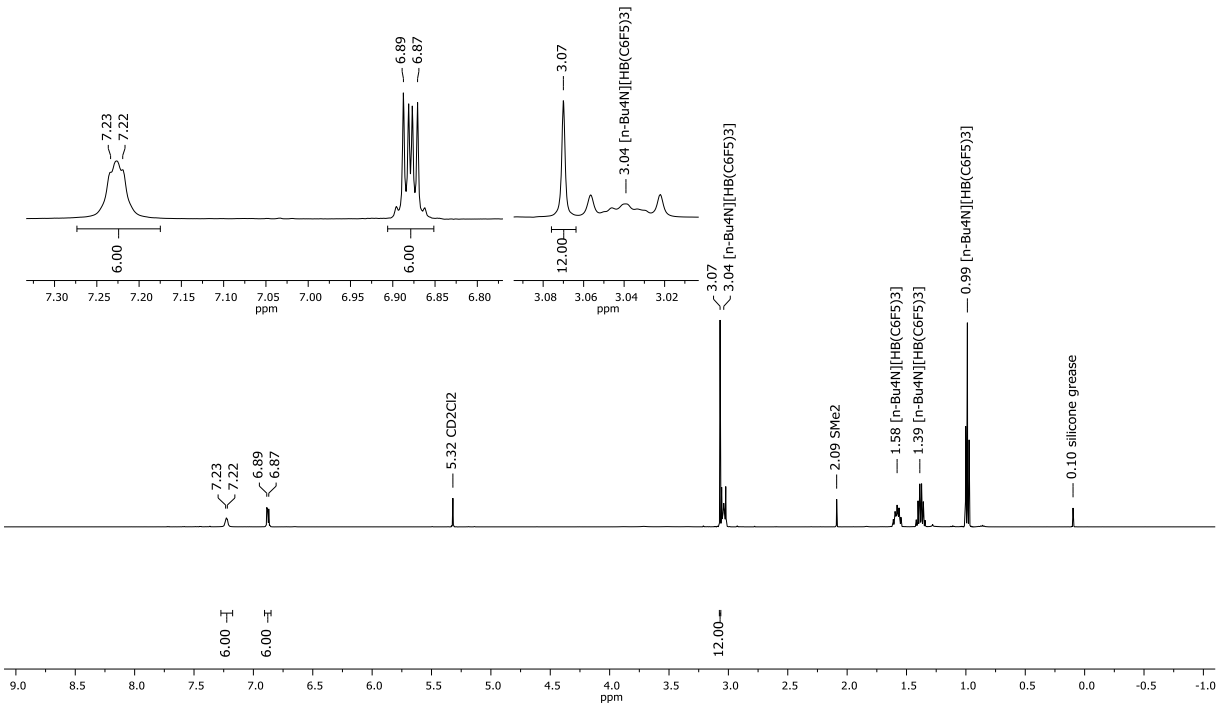

Figure S42. ^{1}H NMR spectrum (500.2 MHz, CD_2Cl_2) of a mixture of **9** and [*n*-Bu_4N][$HB(C_6F_5)_3$].

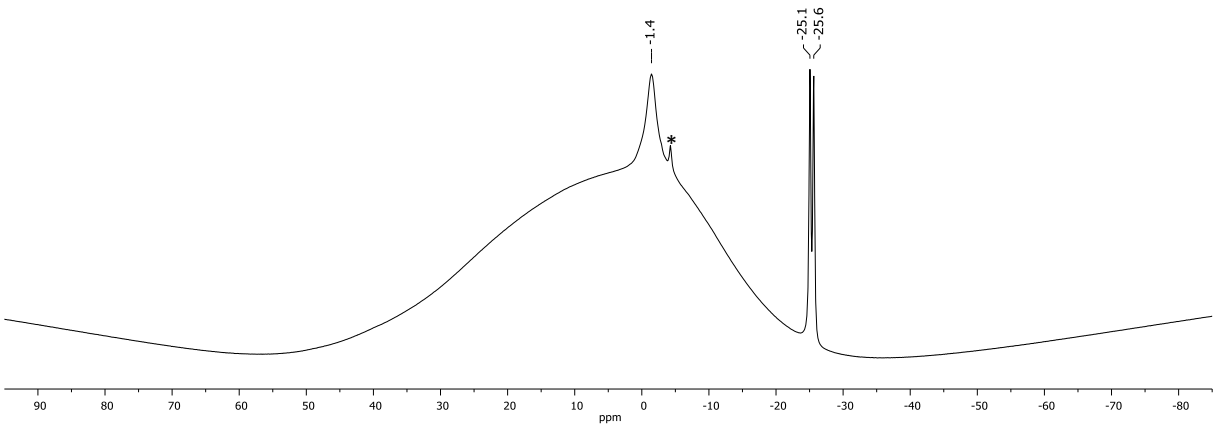

Figure S43. ^{11}B NMR spectrum (160.5 MHz, CD_2Cl_2) of a mixture of **9** and [*n*-Bu_4N][$HB(C_6F_5)_3$]. The resonance marked with (*) corresponds to a minor impurity.

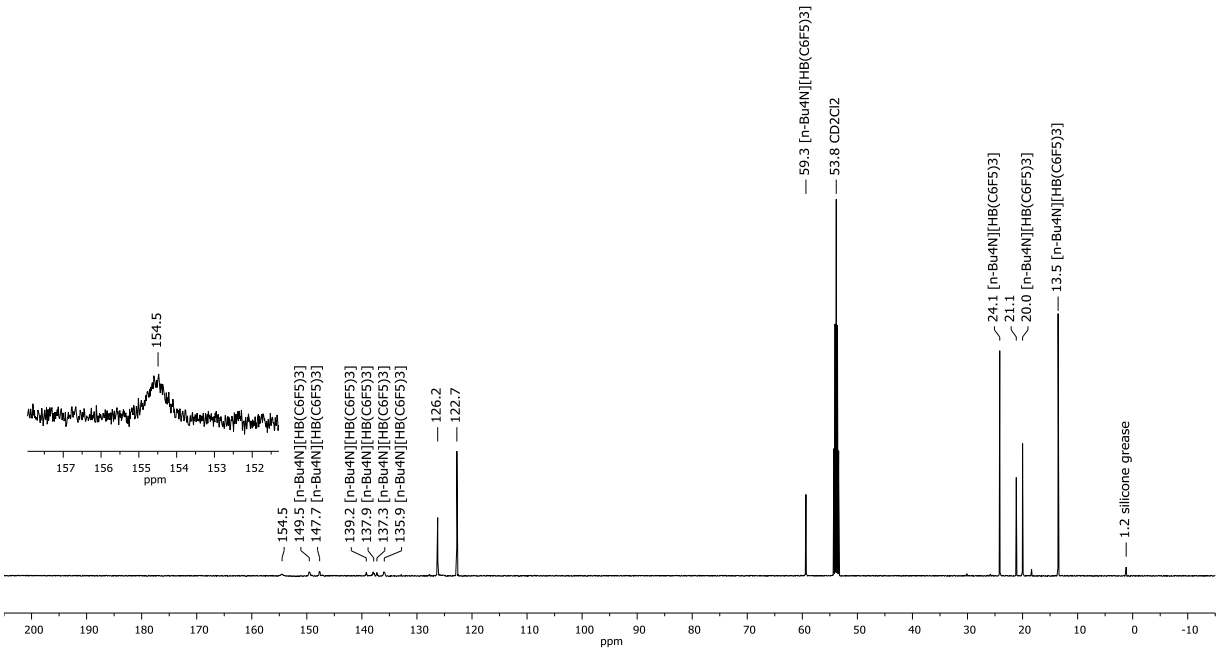

Figure S44. $^{13}C\{^{1}H\}$ NMR spectrum (125.8 MHz, CD_2Cl_2) of a mixture of **9** and [*n*-Bu_4N][$HB(C_6F_5)_3$].

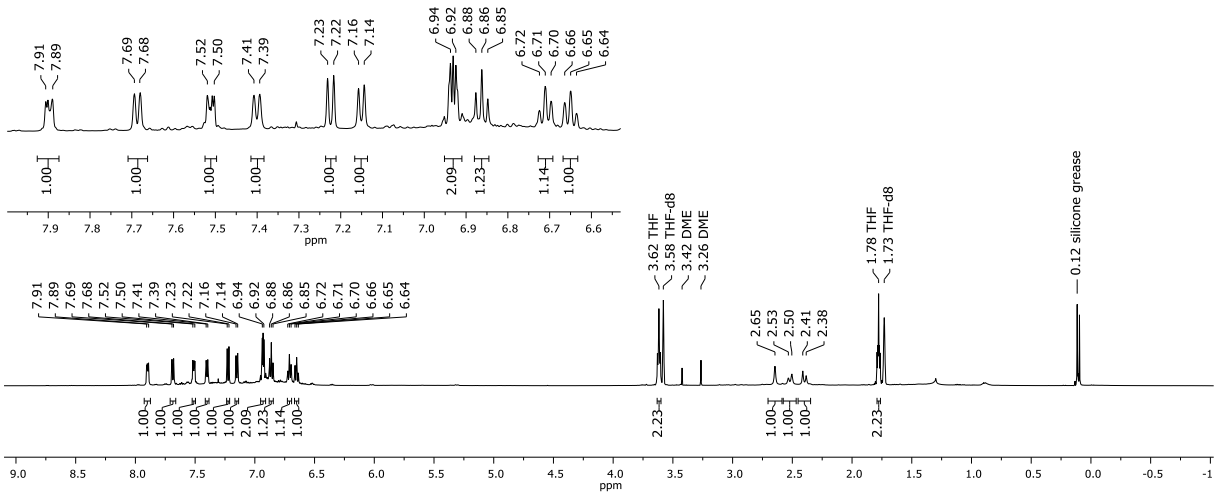

Figure S45. $^{1}H\{^{11}B\}$ NMR spectrum (500.2 MHz, THF-d_8) of [$K_2(thf)_{0.5}$][**10**].

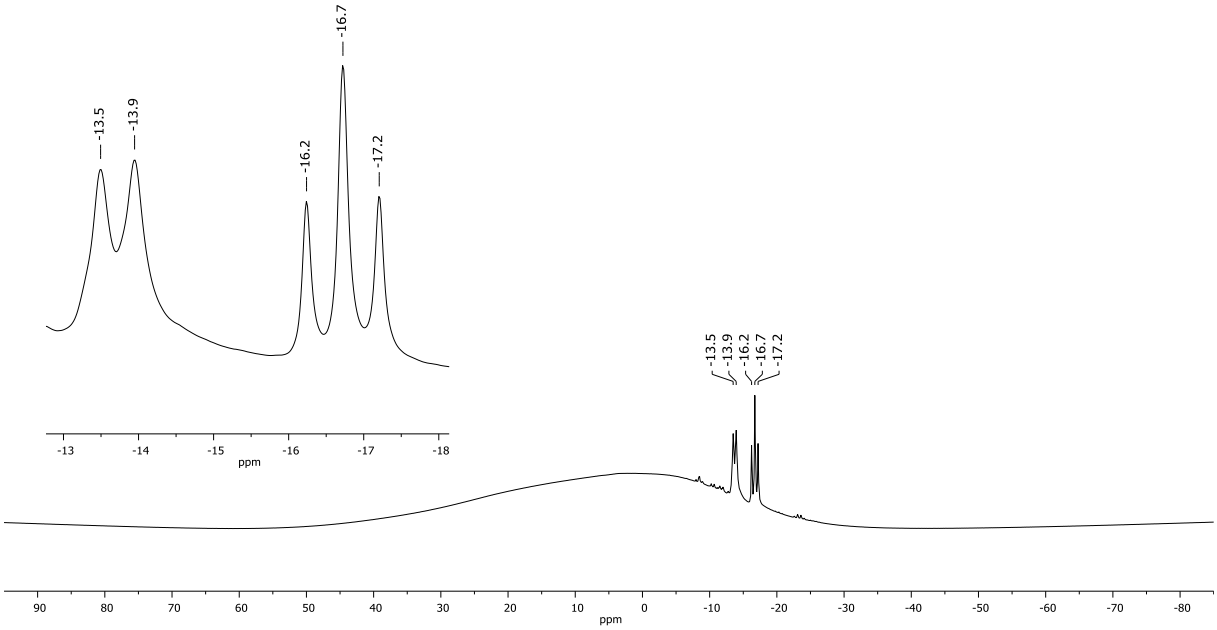

Figure S46. ^{11}B NMR spectrum (160.5 MHz, THF-d_8) of $[K_2(thf)_{0.5}][\mathbf{10}]$.

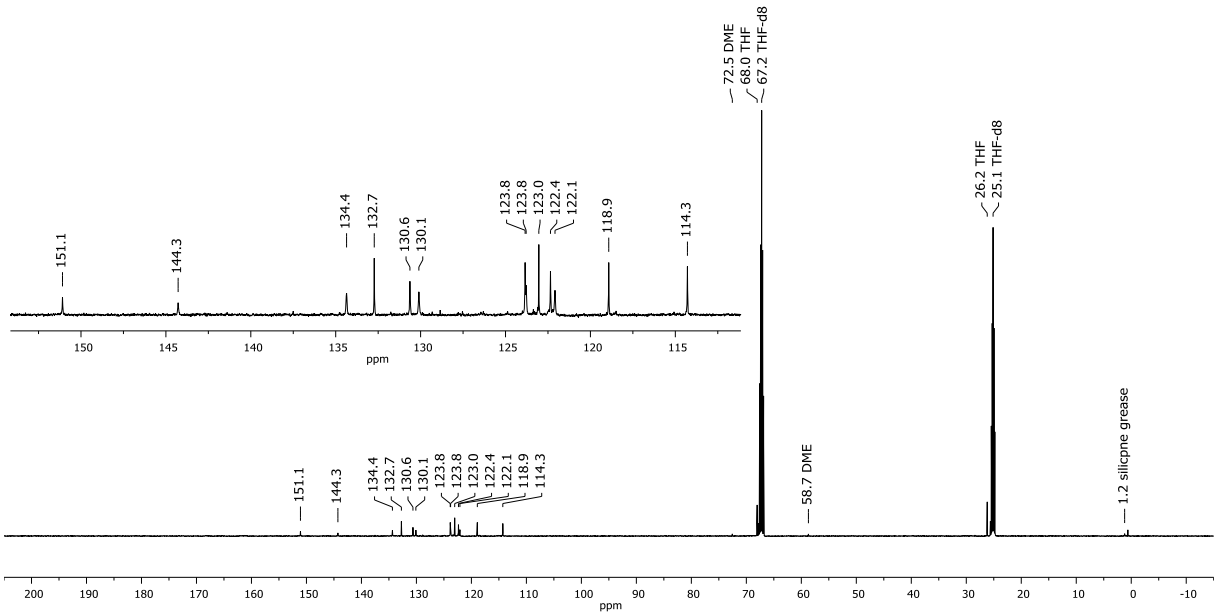

Figure S47. $^{13}C\{^1H\}$ NMR spectrum (125.8 MHz, THF-d_8) of $[K_2(thf)_{0.5}][\mathbf{10}]$.

2.2 Plots of LDI-MS(–) spectra

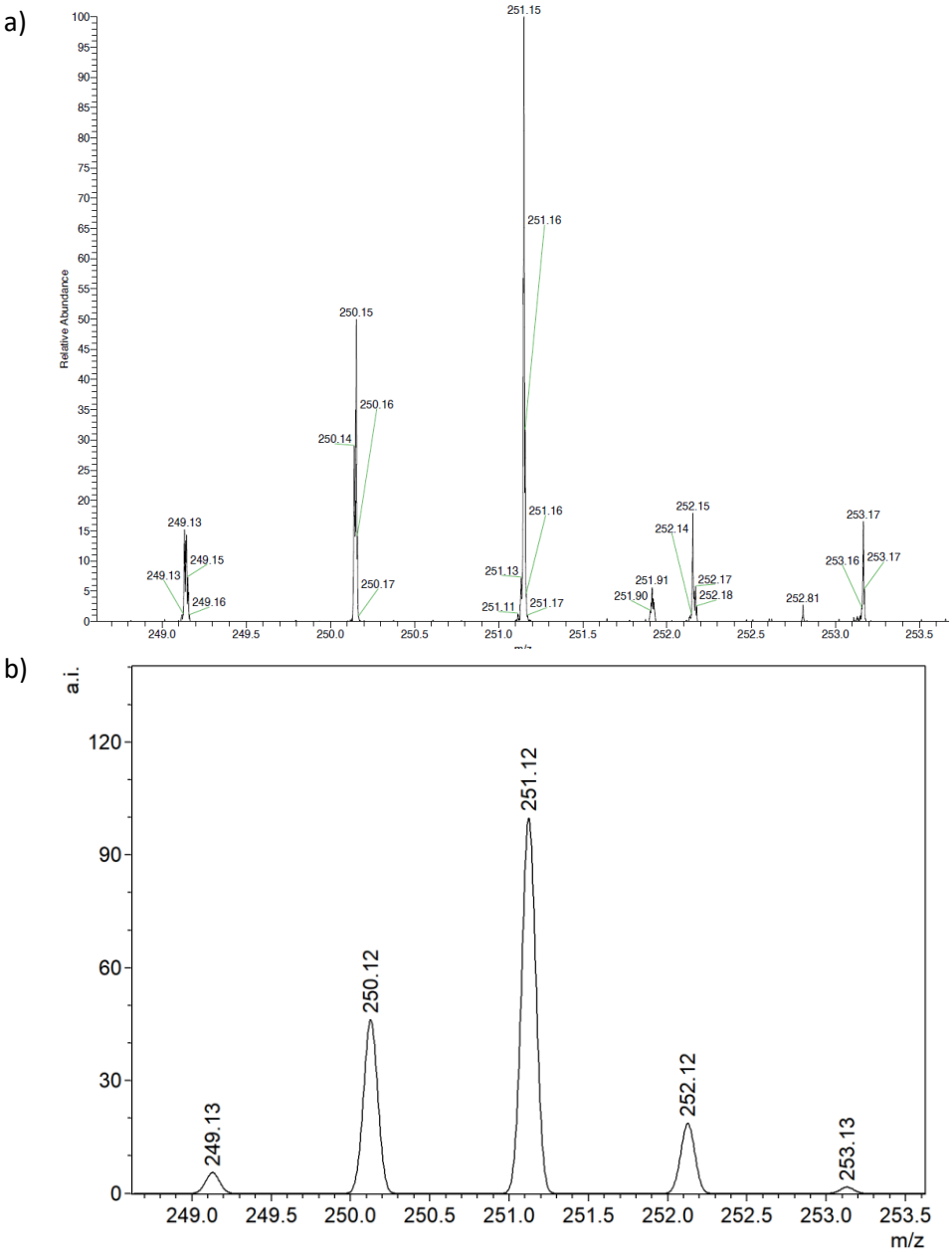

Figure S48. a) Measured ([[**6**] - H]$^-$ = [$C_{18}H_{14}B_2$ - H]$^-$) and b) simulated isotopic pattern of [$C_{18}H_{13}B_2$]$^-$ (measurement on K_2[**6**]).

a)

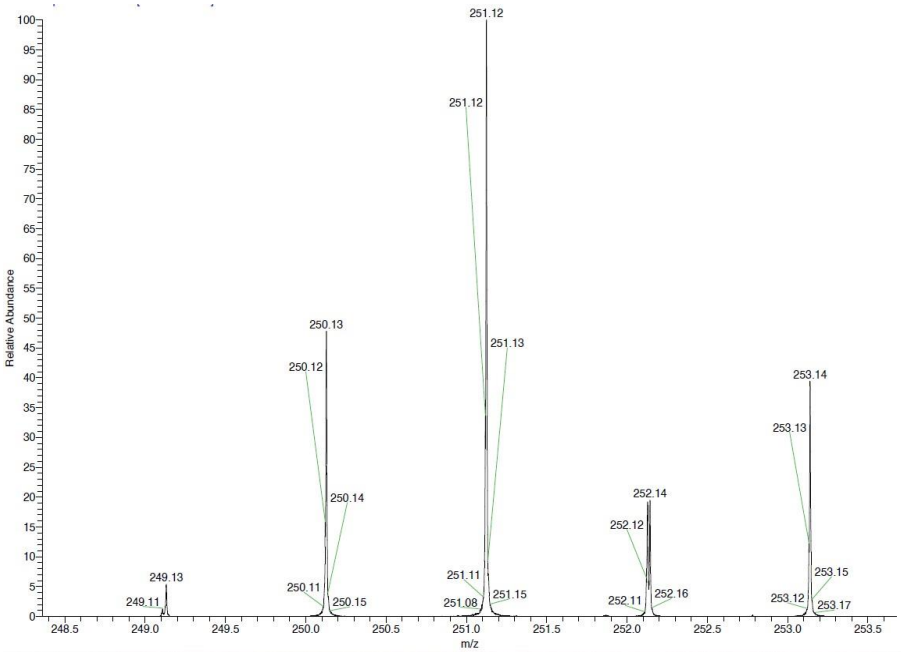

b)

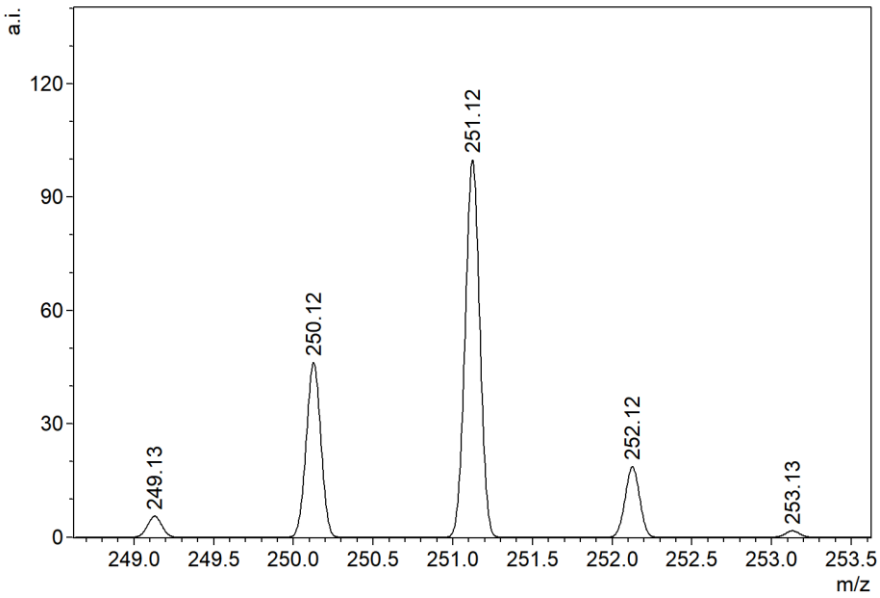

Figure S49. a) Measured ([[**6**] - H]$^-$ = [$C_{18}H_{14}B_2$ - H]$^-$) and b) simulated isotopic pattern of [$C_{18}H_{13}B_2$]$^-$ (measurement on [*n*-Bu_4N]$_2$[**6**]).

a)

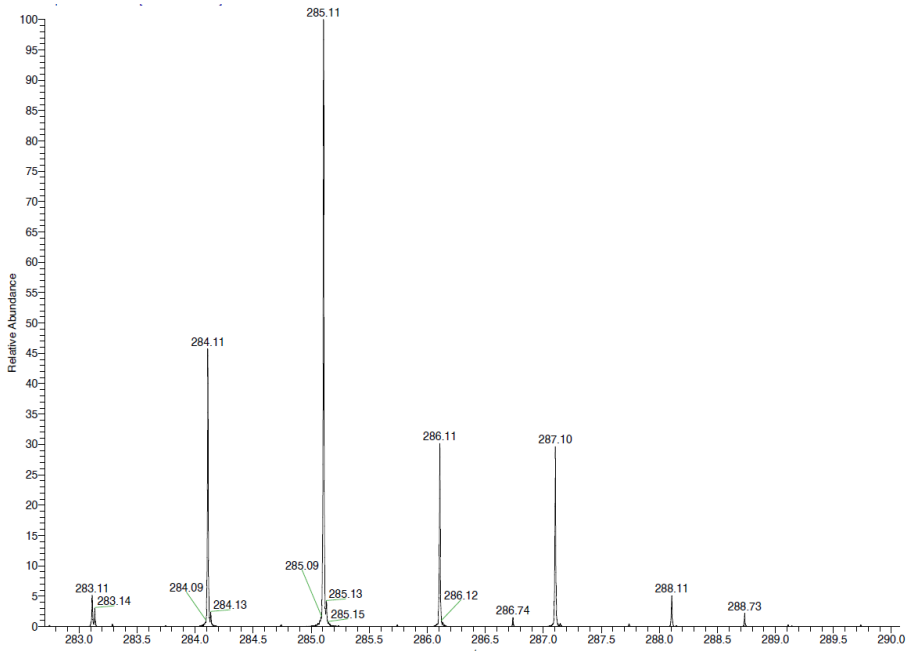

b)

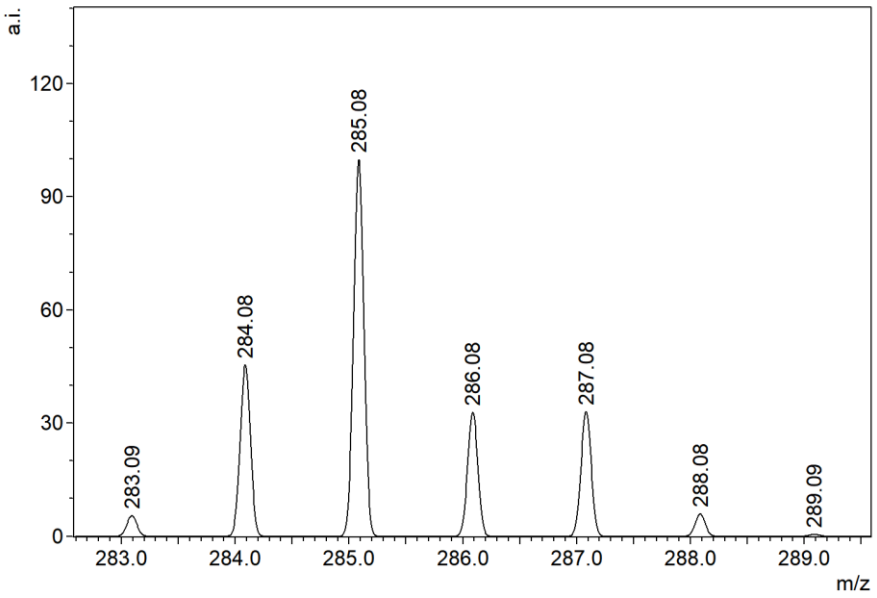

Figure S50. a) Measured ([[**8**] - Cl]$^-$ = [$C_{18}H_{12}B_2Cl_2$ - Cl]$^-$) and b) simulated isotopic pattern of [$C_{18}H_{12}B_2Cl$]$^-$.

a)

b)

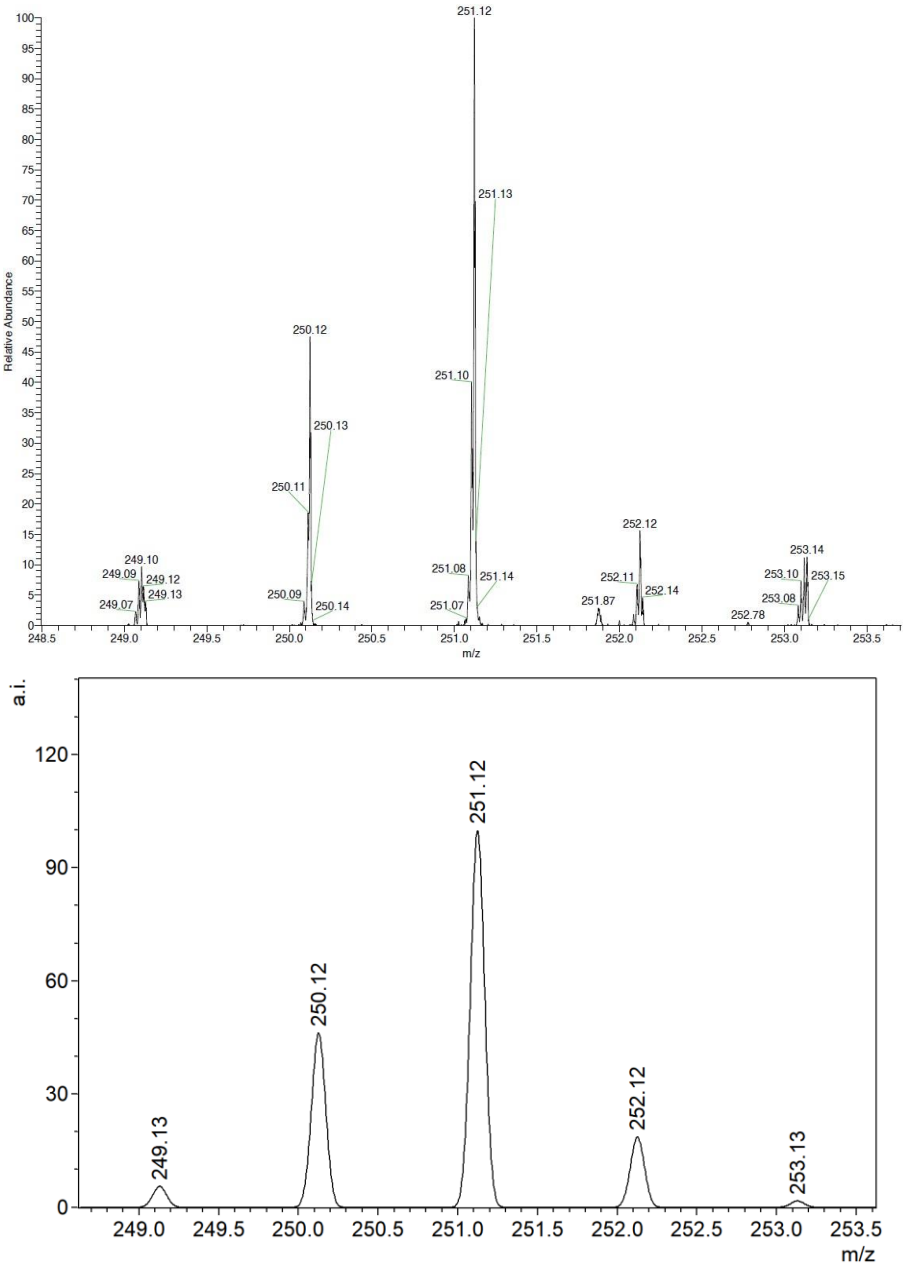

Figure S51. a) Measured ([[**10**] - H]$^-$ = [$C_{18}H_{14}B_2$ - H]$^-$) and b) simulated isotopic pattern of [$C_{18}H_{13}B_2$]$^-$ (measurement on K_2[**10**]).

3. Computational details

Geometry optimizations and Hessian calculations were performed at the ωB97xD[S7]/6-31+G(d,p)[S8] level of theory including implicit solvation by the solvent model based on density (SMD; solvent = THF; ε = 7.4257).[S9] Optimized geometries were confirmed to be the desired minimum energy structures or transition states by vibrational frequency analysis. Single point calculations were performed at the SMD(THF)/ωB97xD/6-311++G(d,p)[S8] level.

Vertical S_1 energies were calculated using TD-DFT; T_1 states were also calculated as vertical energies. To get comparable energies of S_0, S_1, and T_1, all energies were corrected with the same thermal correction term for free energy obtained from the frequency analysis of the respective S_0 geometry. All free energy values were calculated for the corresponding experimental temperature. A concentration correction accounting for the change in standard states going from gas phase to condensed phase was neglected in the given G_{298} values, since there is no change in moles in the course of the computed mechanisms.

^{13}C NMR shift calculations were performed with the gauge-invariant atomic orbital (GIAO) method[S10,11] at the SMD(THF)/ωB97xD/6-311++G(d,p) level. Since the experimentally observed NMR shift values are a result of a dynamic process, the computed isotropic shielding tensors (ISTs) were averaged over all symmetry-related positions of the nuclei under consideration in each molecule. These calculated isotropic shielding tensors were referenced against $SiMe_4$ (optimized at SMD(THF)/ωB97xD/6-31+G(d,p)). The calculated ^{13}C NMR shift values of [**10**]$^{2-}$ were further corrected by applying a compensating linear scaling approach. Based on the benchmark compounds [**6**]$^{2-}$, [**H2BFlu**]$^{-}$, and [**H4DBA**]$^{2-}$ (see section 3.3), we obtained the correction term (**I**) from a linear regression derived from the plot shown in Figure S56 (x-axis: calculated ^{13}C NMR shifts, y-axis: experimentally determined ^{13}C NMR shifts).

$$\delta_{corr}\left(^{13}\mathrm{C}\right) = 0.9602 \cdot \delta_{calc}\left(^{13}\mathrm{C}\right) - 1.0337 \qquad \textbf{(I)}$$

In order to ensure maximum comparability between the individual F^--ion affinities (FIA), the PBE-D3(BJ)[S12–S14]/def2-TZVPP[S15] level of theory was used for geometry optimizations of **S1**, [**S1**(F)]$^-$, [**S2**]$^-$, [**S2**(F)]$^{2-}$, **S3**, [**S3**(F)]$^-$, $[CF_3O]^-$, and CF_2O (Figure S52). This and the PBE0-GD3(BJ)/def2-TZVPPD level of theory have recently been used in a series of related FIA calculations.[S16] The reaction enthalpies of the isodesmic reactions {$[LA]^{n-}$ + $[CF_3O]^-$ → $[LA(F)]^{(n+1)-}$ + CF_2O} (LA = Lewis acid; n = 0, 1) were calculated using the PBE0-GD3(BJ)[S17]/def2-TZVPPD[S15,18] level of theory with or without the conductor-like polarizable continuum model with the COSMO epsilon function (CPCMC; solvent = CH_2Cl_2)[S19] for the inclusion of solvent effects. Final FIAs were obtained after subtracting the experimentally determined FIA of CF_2O (208.8 kJ mol^{-1}) from the calculated reaction enthalpies.

All DFT calculations were performed using *Gaussian 09, Revision D.01*[S20] or *Gaussian 16, Revision B.01*.[S21] Calculations with the CPCMC solvation model were performed using *ORCA 5.0.3*.[S22] Graphical representations of molecular geometries were produced with the *CYLview20* software.[S23]

3.1 Corrected free energy values of computed compounds

[**6**]$^{2-}$
G_{298} = –743.9888636 Hartree

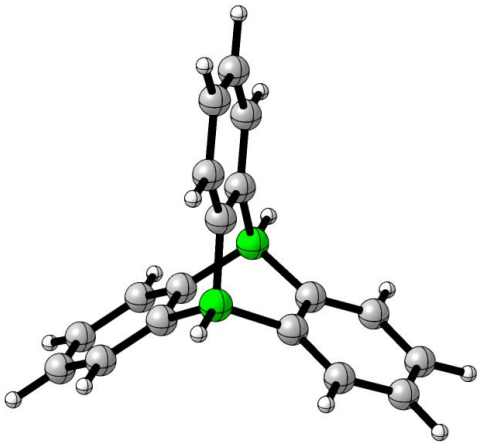

[**TS1**]$^{2-}$
G_{298} = –743.8900717 Hartree

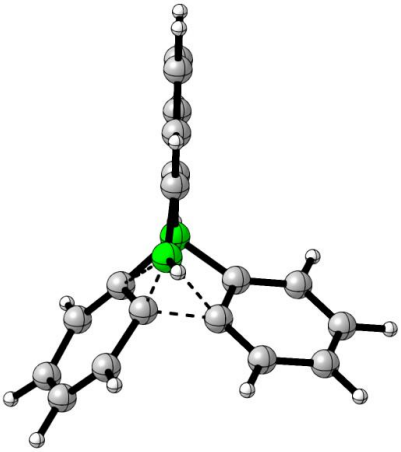

[**Int1**]$^{2-}$
G_{298} = –743.9300315 Hartree

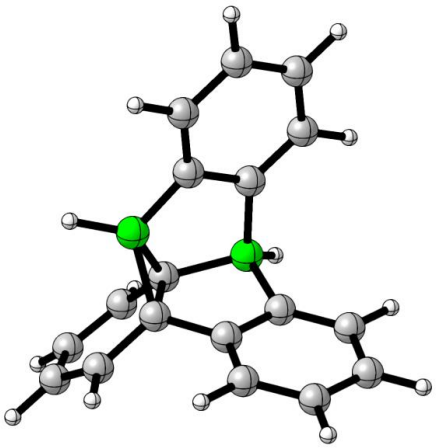

[**TS2**]$^{2-}$
G_{298} = –743.9019693 Hartree

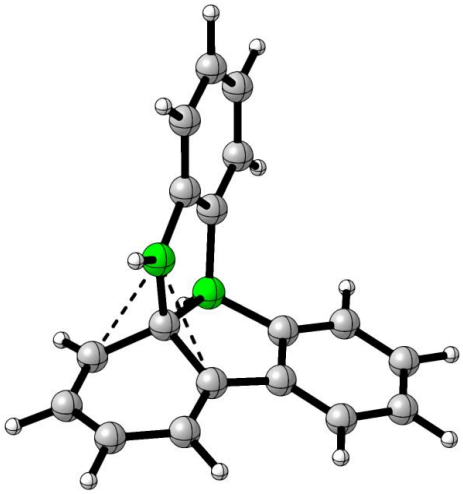

[**Int2**]$^{2-}$
G_{298} = –743.9344163 Hartree

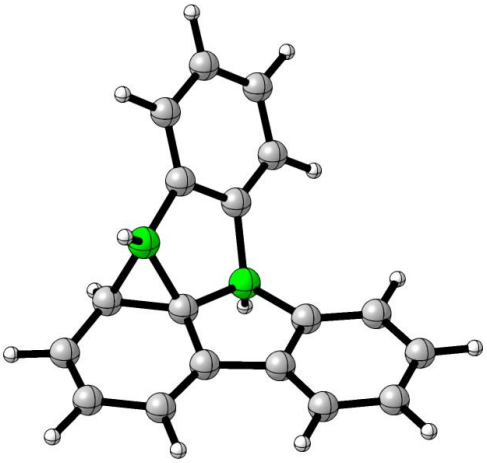

[**TS3**]$^{2-}$
G_{298} = –743.9029222 Hartree

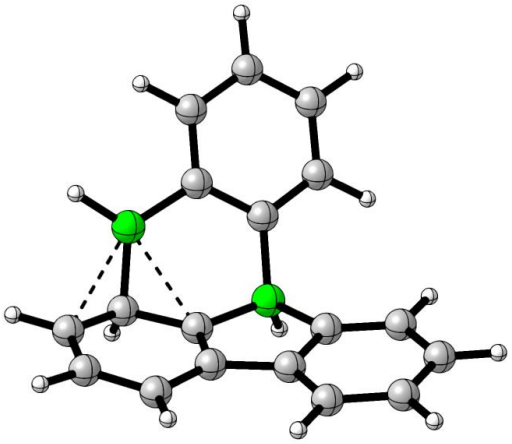

[**Int3**]$^{2-}$
G_{298} = –743.9218368 Hartree

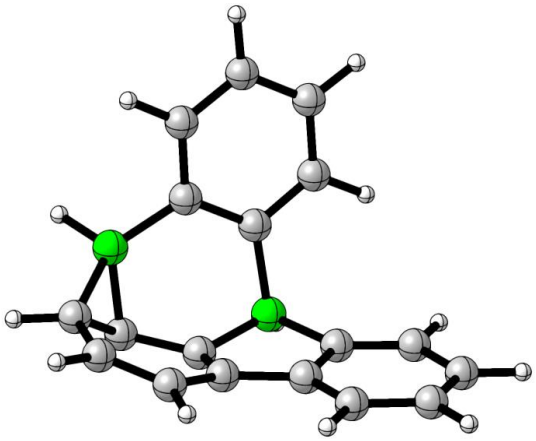

[**TS4**]$^{2-}$
G_{298} = –743.9014916 Hartree

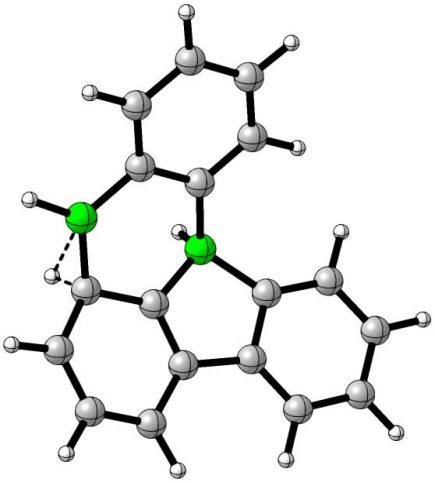

[**10**]$^{2-}$
G_{298} = –743.9883719 Hartree

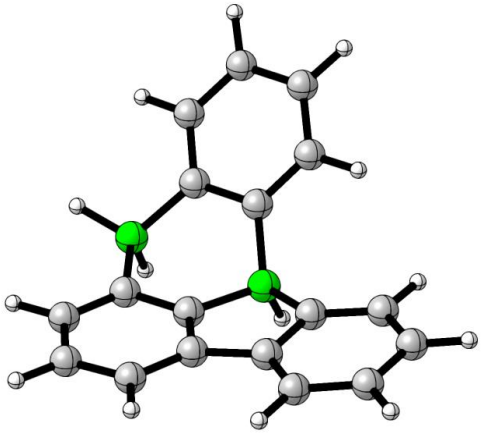

[**Int1'**]$^{2-}$
G_{298} = –743.9061811 Hartree

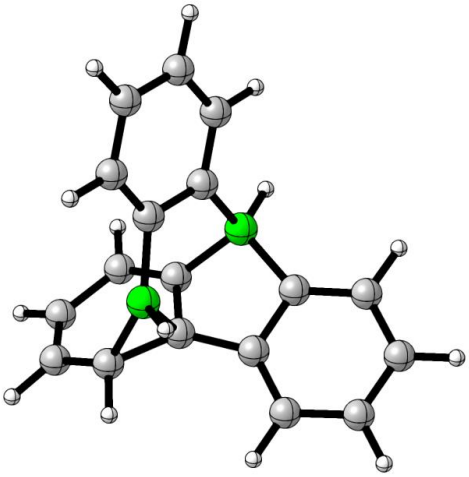

[**TS4'**]$^{2-}$
G_{298} = –743.8701893 Hartree

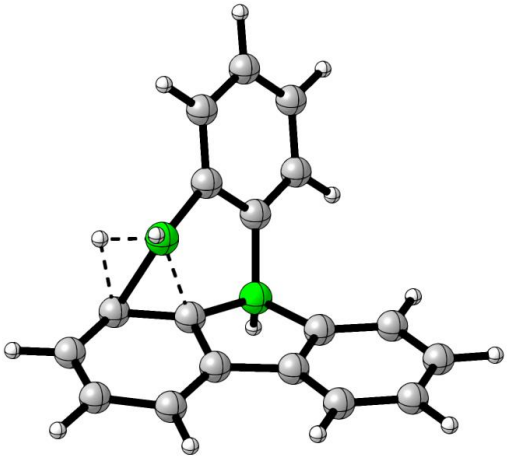

6^{C}
G_{298} = –770.2736806 Hartree

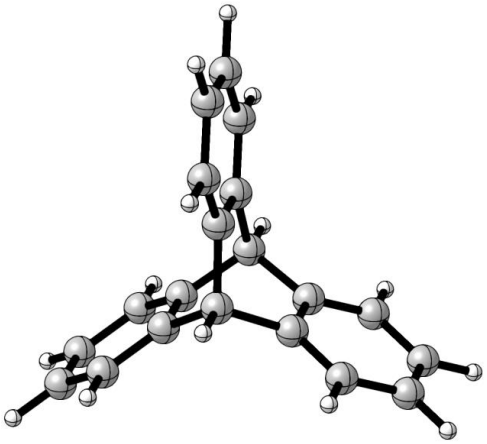

Int1^{C}

G_{298} = –770.2103798 Hartree

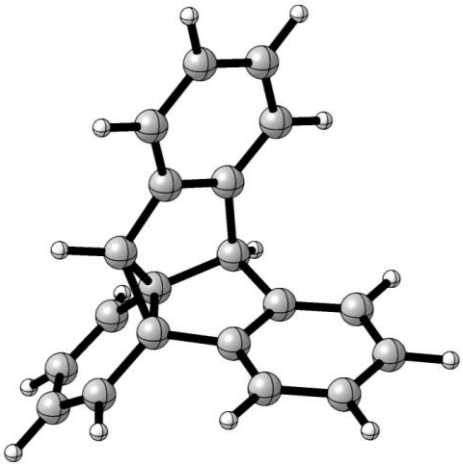

Int2^{C}

G_{298} = –770.2246594 Hartree

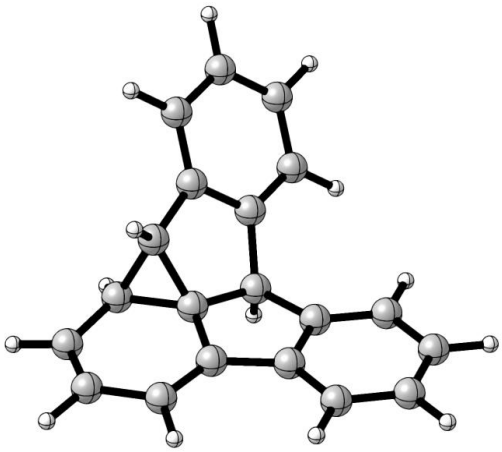

10^{C}

G_{298} = –770.2826870 Hartree

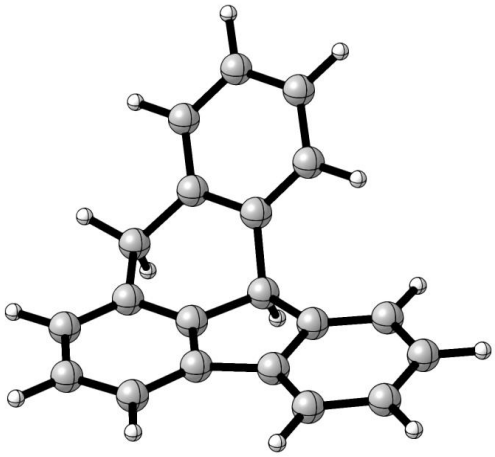

S1

H_{298} = −741.938588 Hartree

$H_{298,CPCMC}$ = –741.950561 Hartree

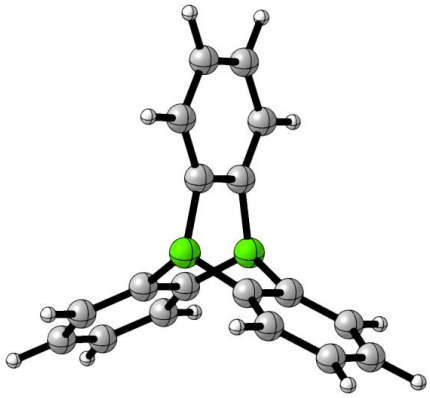

[**S1**(F)]$^{-}$

H_{298} = −841.906919 Hartree

$H_{298,CPCMC}$ = –841.972595 Hartree

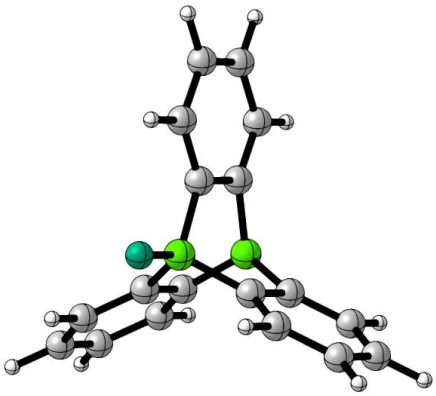

[**S2**]$^{-}$

H_{298} = −742.640134 Hartree

$H_{298,CPCMC}$ = –742.704404 Hartree

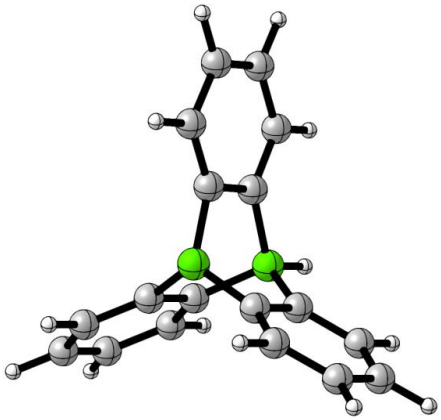

[**S2**(F)]$^{2-}$

H_{298} = −842.467577 Hartree

$H_{298,CPCMC}$ = –842.681943 Hartree

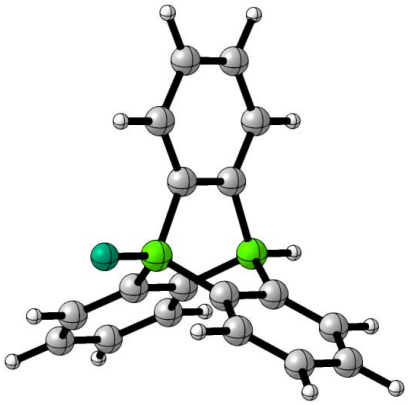

S3

H_{298} = –1219.739025 Hartree

$H_{298,CPCMC}$ = –1219.759085 Hartree

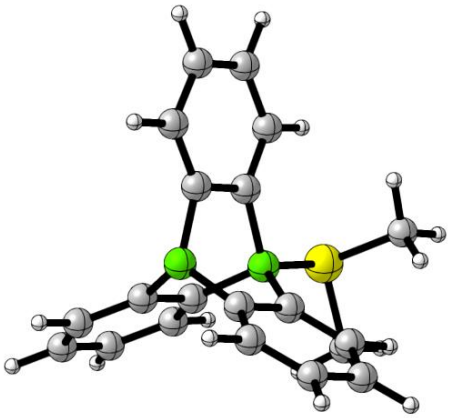

[**S3**(F)]$^{-}$

H_{298} = –1319.685537 Hartree

$H_{298,CPCMC}$ = –1319.758402 Hartree

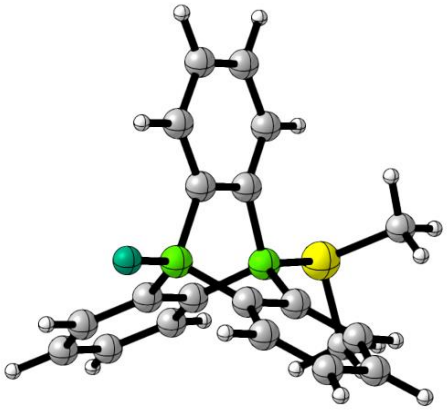

3.2 Computed F^--ion affinities

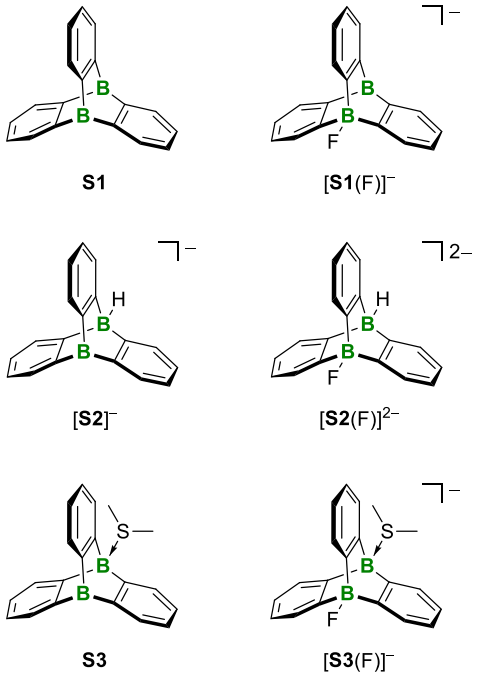

Figure S52. Lewis structures of computed compounds for determination of the FIA.

Table S1. Lewis acidities assessed by F^--ion affinities (gas-phase results); theory level: PBE0-D3(BJ)/def2-TZVPPD.

Compound	*n*	$[LA]^{n-}$ / Hartree	$[CF_3O]^-$ / Hartree	$[LA(F)]^{(n+1)-}$ / Hartree	CF_2O / Hartree	FIA / kJ mol^{-1}
S1	0	−741.938588	−412.708690	−841.906919	−312.832782	451
[**S2**]$^-$	1	−742.640134	−412.708690	−842.467577	−312.832782	82
S3	0	−1219.739025	−412.708690	−1319.685537	−312.832782	394

Table S2. Lewis acidities assessed by F^--ion affinities (results using the CPCMC solvation model); theory level: PBE0-D3(BJ)/def2-TZVPPD/CPCMC(CH_2Cl_2).

Compound	*n*	$[LA]^{n-}$ / Hartree	$[CF_3O]^-$ / Hartree	$[LA(F)]^{(n+1)-}$ / Hartree	CF_2O / Hartree	FIA_{solv} / kJ mol^{-1}
S1	0	–741.950561	–412.790899	–841.972595	–312.835503	384
[**S2**]$^-$	1	–742.704404	–412.790899	–842.681943	–312.835503	267
S3	0	–1219.759085	–412.790899	–1319.758402	–312.835503	324

The calculated FIA_{solv} of **S1** (384 kJ mol^{-1}) is higher than, e.g., that of $B(C_6F_5)_3$ (315 kJ mol^{-1}) or BI_3 (366 kJ mol^{-1}).[S16] As a result, **S1** should be among the strongest boron-based neutral Lewis acids. As soon as one of the boron centers of **S1** is coordinated by a donor ligand, the FIA of the resulting species ([**S2**]$^-$ or **S3**) decreases significantly to 267 and 324 kJ mol^{-1}, respectively. We observe that the

anionic donor H^- leads to a stronger decrease in the FIA compared to the neutral SMe_2 donor. This may be traced back to Coulomb repulsion during F^--adduct formation with [**S2**]$^-$.

Given the affinity trend $FIA_{solv}([\mathbf{S2}]^-) < FIA_{solv}(\mathbf{S3}) \approx FIA_{solv}(B(C_6F_5)_3) < FIA_{solv}(\mathbf{S1})$, a stepwise H^--abstraction/SMe_2-adduct formation scenario seems plausible in the context of the formation of **9** from [*n*-$Bu_4N]_2$[**6**]/ $B(C_6F_5)_3$/SMe_2.

We note that the inclusion of the CPCMC solvation model (solvent = CH_2Cl_2) leads to a decrease in the computed FIA values of the neutral species **S1** and **S3**. However, this trend is inverted for [**S2**]$^-$. This could be attributed to a disproportionately pronounced stabilization of the dianionic [**S2**(F)]$^{2-}$ species when a polar solvent model is used. To validate this assumption, we (i) reproduced the DFT-derived FIA trends for [**S2**]$^-$ using the high-level domain-based local pair natural orbital coupled-cluster DLPNO-CCSD(T) method[S24] (with and without solvent model) and (ii) calculated the FIA of [**S2**]$^-$ applying a less polar solvent model (*n*-hexane). This gave only a small increase in the FIA value compared to the gas phase calculations, indicating that the observed effect is indeed caused by a specific dianion effect resulting from the polar solvation model.

Table S3. F^--ion affinities of [**S2**]$^-$ computed on different levels of theory and with/without CPCMC solvation model (*n*-hexane or CH_2Cl_2).

Level of theory	**[S2]$^-$ / Hartree**	**[CF_3O]$^-$ / Hartree**	**[S2(F)]$^{2-}$ / Hartree**	**CF_2O / Hartree**	**FIA_{solv} / kJ mol^{-1}**
PBE0-D3(BJ)/def2-TZVPPD	–742.640134	–412.708690	–842.467577	–312.832782	82
PBE0-D3(BJ)/def2-TZVPPD/CPCMC(*n*-hexane)	–742.667956	–412.745040	–842.560536	–312.85176	160
PBE0-D3(BJ)/def2-TZVPPD/CPCMC(CH_2Cl_2)	–742.704404	–412.790899	–842.681943	–312.835503	267
DLPNO-CCSD(T)/(aug)-cc-pVDZ	–741.213261	–412.128414	–840.914986	–312.383640	96
DLPNO-CCSD(T)/(aug)-cc-pVDZ/CPCMC (CH_2Cl_2)	–741.274898	–412.210361	–841.126631	–312.386165	281

3.3 Computational characterization of the photoisomerization pathway in excited states

The energies of the proposed photoisomerization mechanism were computed not only in the S_0 state, but also the energies of the vertical T_1 and S_1 excited states have been calculated (see Figure S53).

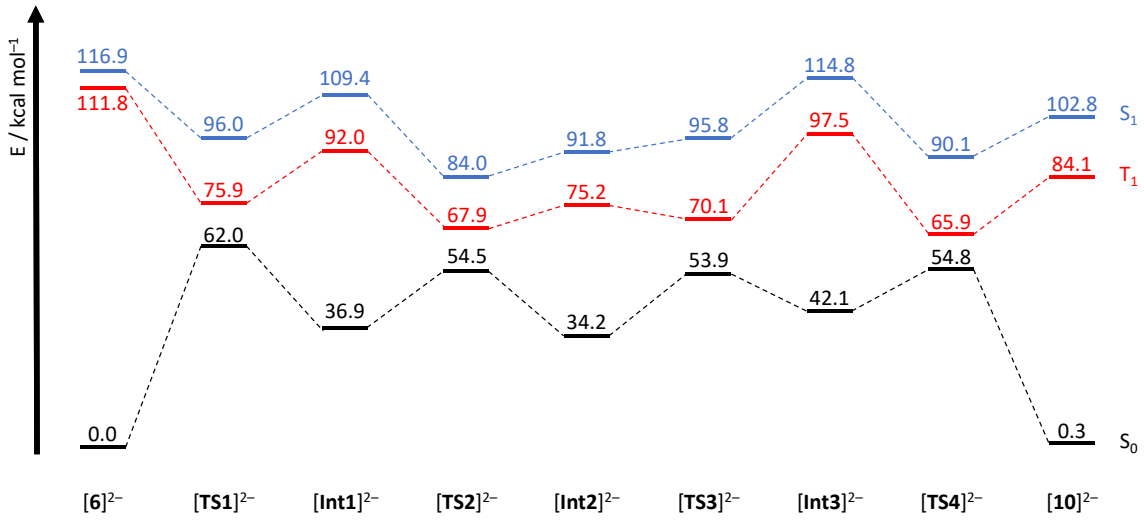

Figure S53. Proposed pathways for the photoisomerization of [**6**]$^{2-}$ to [**10**]$^{2-}$ in the S_0 (black), T_1 (red), and S_1 states (blue).

For the final C–H activation step, we found not only [**TS4**]$^{2-}$ (from [**Int3**]$^{2-}$), but also an alternative [**TS4'**]$^{2-}$ (from [**Int2**]$^{2-}$). [**TS4'**]$^{2-}$ lies at +74.5 kcal mol^{-1} (referenced to [**6**]$^{2-}$) and is located +40.3 kcal mol^{-1} above [**Int2**]$^{2-}$, which makes C–H activation via [**TS4'**]$^{2-}$ unfavorable compared to [**TS4**]$^{2-}$ (Figure S54).

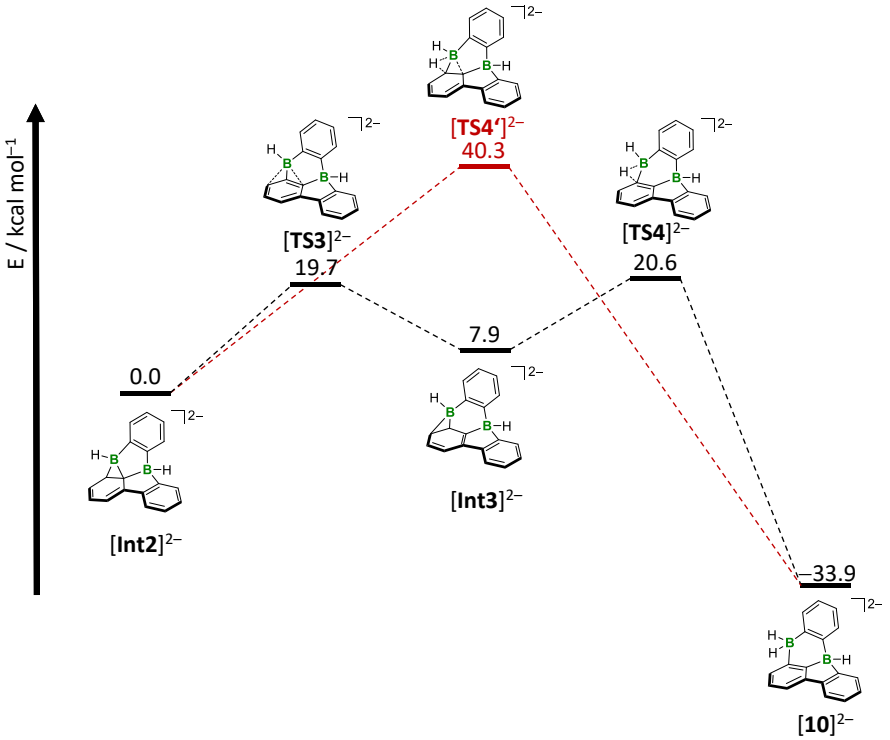

Figure S54. Two possible pathways from [**Int2**]$^{2-}$ to [**10**]$^{2-}$. [**Int2**]$^{2-}$ was set to 0.0 kcal mol^{-1}. The red pathway via [**TS4'**]$^{2-}$ has a barrier of 40.3 kcal mol^{-1}, which makes the black pathway (via [**TS3**]$^{2-}$, [**Int3**]$^{2-}$, and [**TS4**]$^{2-}$, highest barrier: 19.7 kcal mol^{-1}, highest transition state: [**TS4**]$^{2-}$ at 20.6 kcal mol^{-1}) more favorable.

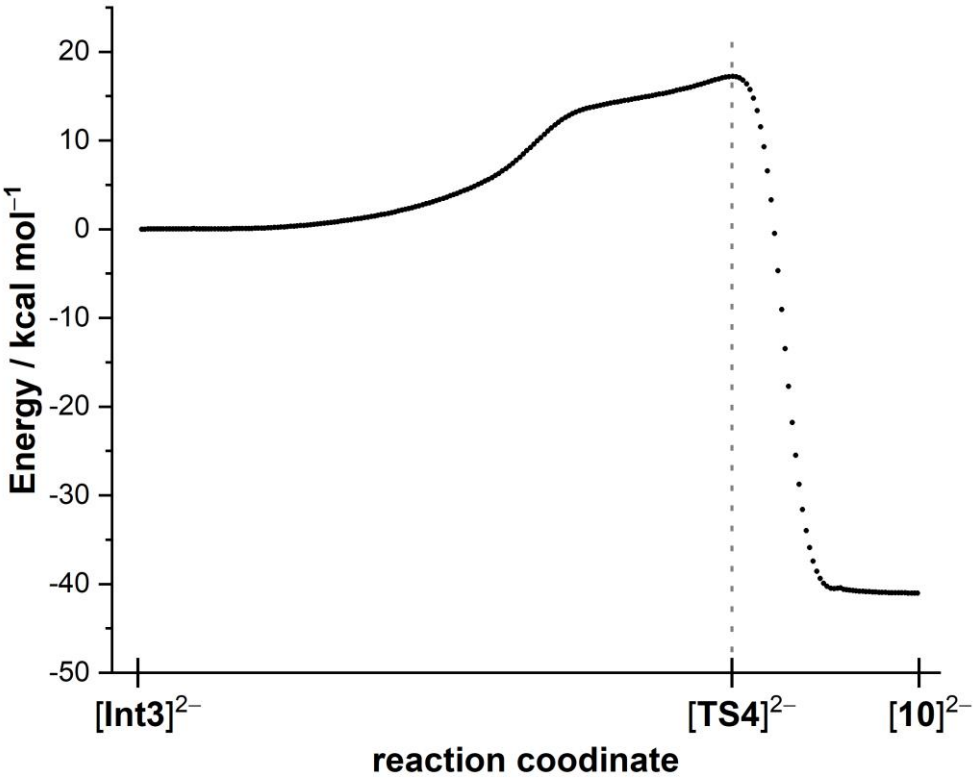

Figure S55. IRC scan calculated for [**TS4**]$^{2-}$. The energy profile shows a plateau between [**Int3**]$^{2-}$ and [**TS4**]$^{2-}$, which could be an indication for a bifurcation mechanism.

3.4 ^{13}C NMR shift calculations for $[10]^{2-}$

Structures and isotropic shielding tensors (IST) relevant to the ^{13}C NMR shift calculations

$SiMe_4$

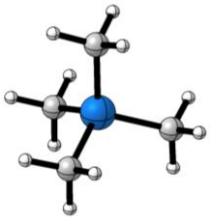

[H2BFlu]$^{-}$

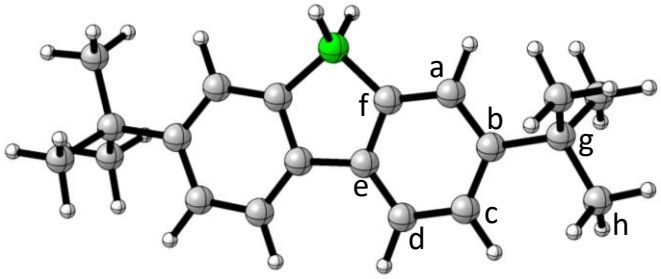

[H4DBA]$^{2-}$

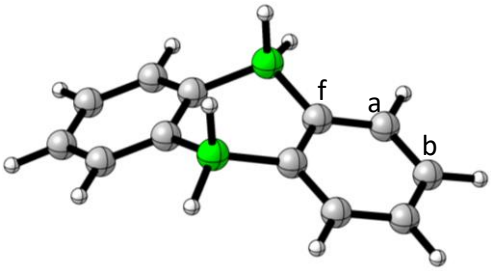

Table S4. Overview on the isotropic shielding tensors (IST), $\delta_{calc}(^{13}C)$ and $\delta_{exp}(^{13}C)$ values of the benchmark set [**6**]$^{2-}$, [**H2BFlu**]$^{-}$, and [**H4DBA**]$^{2-}$. The $\delta_{exp}(^{13}C)$ values are those of the respective K^+ salts. Note that the quarternary C-f atoms of [**H4DBA**]$^{2-}$ were omitted from the study, since no experimental ^{13}C NMR shift has been reported.

IST $\delta_{calc}(^{13}C)$ $\delta_{exp}(^{13}C)$ **[ppm]**	[**6**]$^{2-}$	[**H2BFlu**]$^{-}$	[**H4DBA**]$^{2-}$
a	55.6134 134.5 130.0	54.0248 136.1 128.7	52.8732 137.2 134.9
b	64.2549 125.9 120.6	34.5804 155.5 145.8	63.3853 126.7 122.4
c	-	63.2382 126.9 120.2	-
d	-	65.4626 124.7 118.0	-
e	-	36.0049 154.1 147.0	-
f	10.7314 179.4 169.6	16.0757 174.0 165.9	-
g	-	150.3351 39.8 34.9	-
h	-	156.3408 33.8 32.3	-

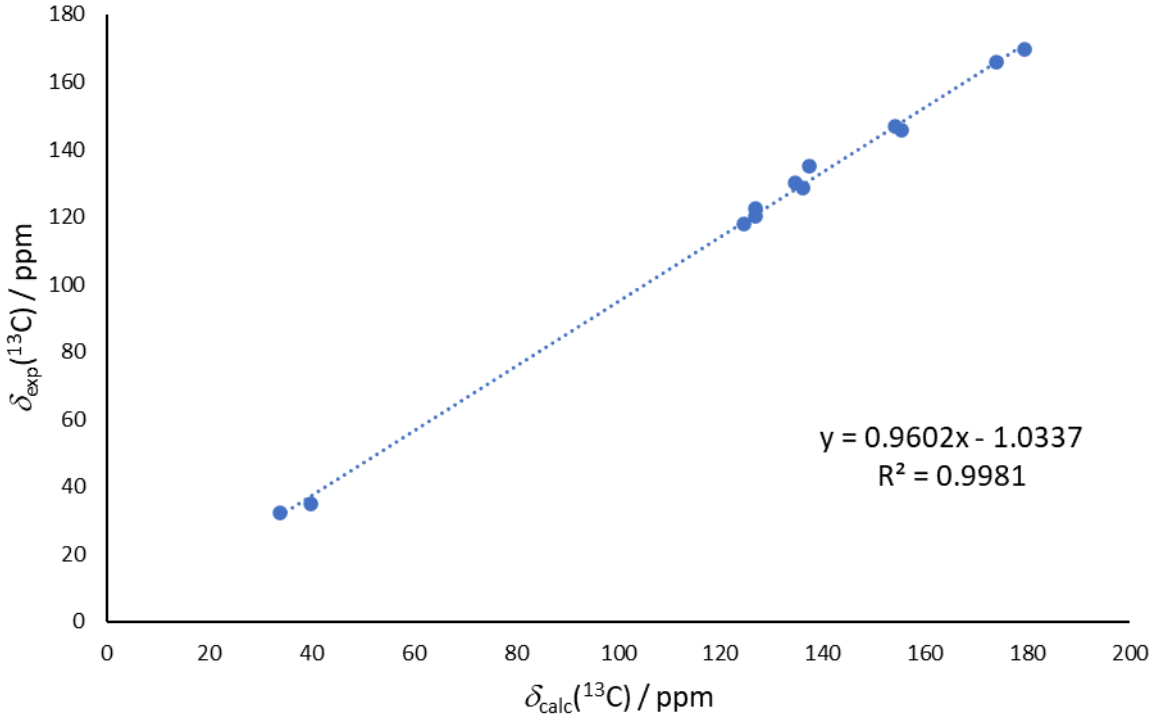

Figure S56. Plot of calculated (x-axis) vs. experimental (y-axis) ^{13}C NMR shifts of [**6**]$^{2-}$, [**H4DBA**]$^{2-}$, and [**H2BFlu**]$^{-}$ to determine a linear empirical correction term for ^{13}C NMR shift calculations on [**10**]$^{2-}$. A linear regression was performed to obtain the term.

Calculation of the ^{13}C NMR shifts of $[10]^{2-}$

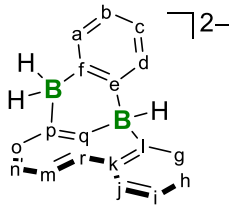

Figure S57. Numbering scheme of [**10**]$^{2-}$.

Table S5. Calculated isotropic shielding tensors (IST), calculated (δ_{calc}), corrected (δ_{corr}), and experimental ^{13}C NMR chemical shifts (δ_{exp}; respective K^+ salts) of [**10**]$^{2-}$ and a comparison of corrected and experimental shift values. All values are given in ppm.

C atom	IST($[10]^{2-}$)	δ_{calc}($[10]^{2-}$)	δ_{corr}($[10]^{2-}$)	δ_{exp}($[10]^{2-}$)	$\Delta\delta_{corr-exp}$
a	50.9008	139.2	132.6	130.6	2.0
b	63.4247	126.7	120.6	122.4	–1.8
c	62.9615	127.2	121.1	122.1	–1.0
d	55.1502	135.0	128.6	134.4	–5.8
e	18.3003	171.8	163.9	165.5	–1.6
f	13.1609	177.0	168.9	161.7	7.2
g	50.6635	139.5	132.9	132.7	0.2
h	60.0309	130.1	123.9	123.8	0.1
i	60.7592	129.4	123.2	123.0	0.2
j	64.9411	125.2	119.2	118.9	0.3
k	30.2122	159.9	152.5	151.1	1.4
l	12.2173	177.9	169.8	167.9	1.9
m	72.0315	118.1	112.4	114.3	–1.9
n	61.6367	128.5	122.3	123.8	–1.5
o	55.0022	135.1	128.7	130.1	–1.4
p	18.9802	171.1	163.3	161.7	1.6
q	6.9033	183.2	174.9	173.0	1.9
r	41.9104	148.2	141.3	144.3	–3.0

The data provided in Table S5 show good agreement of δ_{corr}(^{13}C) with δ_{exp}(^{13}C) of [**10**]$^{2-}$. The deviation from the experimental values is ±2 ppm.

4. X-ray crystal structure determinations

Single-crystal diffraction data were collected at –100 °C on a STOE IPDS II two-circle diffractometer equipped with a *Genix 3D HS* microfocus MoK_α X-ray source (λ = 0.71073 Å). The finalizations of the data, including the empirical absorption corrections, were done using the X-Area v.1.50 (for $[K_2(dme)_3]$[**3**], $[Li(thf)_2]$[**4**], [K(dme)][$K(dme)_2$][**6**], and [K(dme)][$K(dme)_2$][**7**]) or, for **9**·CH_2Cl_2, with the *CrysAlisPro* software v.1.171.42.43a (Rigaku Oxford Diffraction, 2022). The structures were solved using the programs *SHELXS* or *SHELXT* and refined against $|F|^2$ with full-matrix least-squares techniques using the program *SHELXL*-2018/3.[S25,26] All hydrogen atoms were located geometrically and refined riding on the pivot atom.

CIF files containing the crystallographic information were deposited in the Cambridge Crystallographic Data Centre under the deposition codes CSD2238019–CSD2238023 and can be obtained free of charge via www.ccdc.cam.ac.uk/data_request/cif. Crystallographic data and parameters of the diffraction experiments are given in Tables S6 and S7.

Table S6. Crystallographic data and experimental details of $[K_2(dme)_3]$[**3**], $[Li(thf)_2]$[**4**], and [K(dme)][$K(dme)_2$][**6**].

	$[K_2(dme)_3]$[3]	**$[Li(thf)_2]$[4]**	**[K(dme)][$K(dme)_2$][6]**
Deposition code	2238019	2238020	2238021
Chemical formula	$C_{42}H_{60}B_2K_2O_6$	$C_{28}H_{34}B_2ILiO_2$	$C_{30}H_{44}B_2K_2O_6$
M_r	760.72	558.01	600.47
Crystal system, space group	Triclinic, $P\bar{1}$	Triclinic, $P\bar{1}$	Orthorhombic, $P2_12_12_1$
Temperature (K)	173	173	173
a, b, c (Å)	9.5281(6), 11.0226(7), 11.2386(7)	8.4929(3), 9.7032(3), 16.0667(6)	12.8057(7), 14.5978(9), 17.7056(14)
α, β, γ(°)	102.796(5), 97.883(5), 112.732(5)	85.041(3), 82.312(3), 84.756(3)	90, 90, 90
V (Å^3)	1028.54(12)	1302.94(8)	3309.8(4)
Z	1	2	4
F(000)	408	568	1280
Radiation type	Mo $K\alpha$	Mo $K\alpha$	Mo $K\alpha$
μ (mm^{-1})	0.28	1.25	0.32
Crystal shape	Block	Block	Block
Color	Black	Colorless	Colorless
Crystal size (mm)	0.56 × 0.29 × 0.17	0.26 × 0.22 × 0.14	0.28 × 0.28 × 0.26
T_{min}, T_{max}	0.411, 1.000	0.544, 1.000	0.534, 1.000
No. of measured, independent, and observed [$I > 2s(I)$] reflections	14112, 3854, 3447	24727, 5723, 5442	11918, 6187, 5840
R_{int}	0.037	0.024	0.033
Θ values (°), max, min	25.7, 3.2	27.1, 3.3	25.6, 3.5
Range of h, k, l	h = –11→11, k = –13→13, l = –13→13	h = –10→10, k = –12→12, l = –20→20	h = –15→15, k = –15→17, l = –21→18
$R[F^2 > 2s(F^2)]$, $wR(F^2)$, S	0.047, 0.114, 1.19	0.023, 0.061, 1.06	0.033, 0.085, 1.03
No. of reflections	3854	5723	6187
No. of parameters	238	318	369
No. of restraints	0	12	0
$\delta\rho_{max}$, $\delta\rho_{min}$ (e Å^{-3})	0.28, –0.26	0.42, –0.27	0.39, –0.18
Absolute structure parameter		-	–0.02(3)

Table S7. Crystallographic data and experimental details of [K(dme)][K(dme)$_2$][**7**] and **9**·CH_2Cl_2.

	[K(dme)][K(dme)$_2$][7]	**9·CH_2Cl_2**
Deposition code	2238022	2238023
Chemical formula	$C_{40}H_{44}B_2KO_2 \cdot C_8H_{20}KO_4$	$C_{22}H_{24}B_2S_2 \cdot CH_2Cl_2$
M_r	836.81	459.08
Crystal system, space group	Monoclinic, $P2_1/n$	Monoclinic, $P2_1/n$
Temperature (K)	173	173
a, b, c (Å)	9.4510(3), 27.0259(12), 18.2350(7)	12.7930(4), 10.3041(2), 18.5280(5)
α, β, γ(°)	90, 102.177(3), 90	90, 108.578(3), 90
V (Å^3)	4552.8(3)	2315.08(12)
Z	4	4
F(000)	1792	960
Radiation type	Mo $K\alpha$	Mo $K\alpha$
μ (mm^{-1})	0.26	0.47
Crystal shape	Plate	Prism
Color	Colorless	Colorless
Crystal size (mm)	0.24 × 0.14 × 0.08	0.21 × 0.17 × 0.16
T_{min}, T_{max}	0.445, 1.000	0.704, 1.000
No. of measured, independent, and observed [I > 2s(I)] reflections	45836, 8880, 6884	26257, 5084, 4085
R_{int}	0.052	0.062
Θ values (°), max, min	26.0, 2.3	27.1, 3.9
Range of h, k, l	h = –11→11, k = –33→33, l = –22→22	h = –16→16, k = –13→13, l = –23→23
$R[F^2 > 2s(F^2)]$, $wR(F^2)$, S	0.050, 0.111, 1.06	0.037, 0.104, 1.02
No. of reflections	8880	5084
No. of parameters	529	284
No. of restraints	0	6
$\delta\rho_{max}$, $\delta\rho_{min}$ (e Å^{-3})	0.24, –0.22	0.34, –0.38

4.1 Single-Crystal X-ray Analysis of $[K_2(dme)_3][3]$

Compound $[K_2(dme)_3][\mathbf{3}]$ crystallizes in the triclinic space group $P\bar{1}$ (No. 2; Figure S58). The boron-containing anion lies on an inversion center ((a) in Figure S58). The K^+ cation coordinates the anion with weak $K\cdots\pi(C_6)$ interactions ($K\cdots C$ distances: 3.0198(19) – 3.164(2) Å). Its coordination sphere is completed by one chelating and one $K^+\cdots K^+$-bridging dme ligand ((b) in Figure S58).

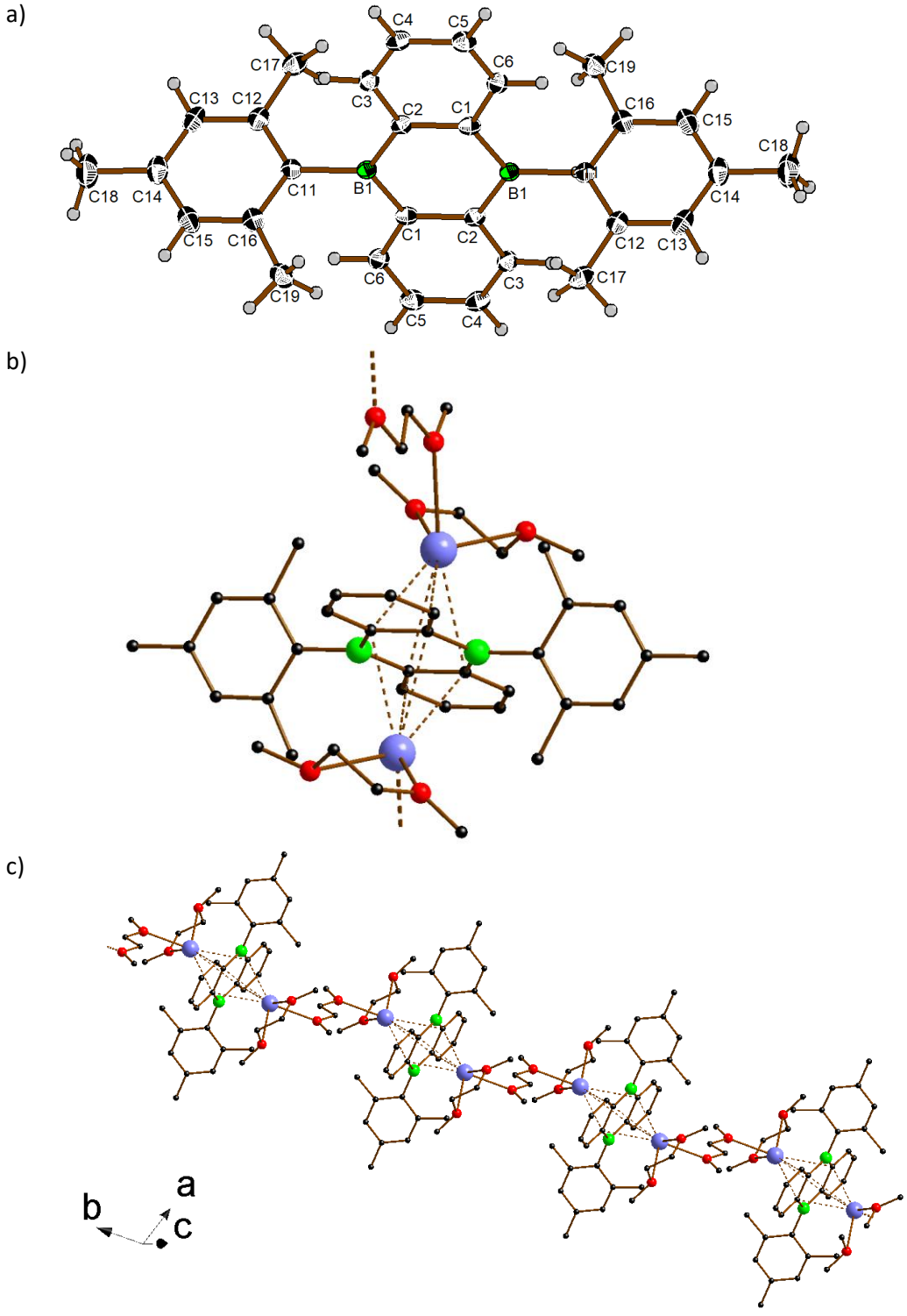

Figure S58. a) Molecular structure of the anion $[\mathbf{3}]^{2-}$ in the solid state; atomic displacement ellipsoids are drawn at the 50% probability level. b) Coordination of the K^+ cations (light blue spheres) in $[K_2(dme)_3]$ $[\mathbf{3}]$; H atoms are omitted for clarity. Note that the $[\mathbf{3}]^{2-}$ dianion lies on an inversion center. c) Coordination polymer of $[K_2(dme)_3][\mathbf{3}]$ in the crystal lattice.

4.2 Single-Crystal X-ray Analysis of [Li(thf)$_2$][4]

Compound [Li(thf)$_2$][**4**] crystallizes in the triclinic space group $P\bar{1}$ (No. 2; Figure S59). The Li^+ cation coordinates the anion by an Li–I bond and weak Li···π(C_6) interactions (Li···C distances: 2.624(4) – 2.722(4) Å). Its coordination sphere is completed by two thf ligands, one of which is conformationally disordered.

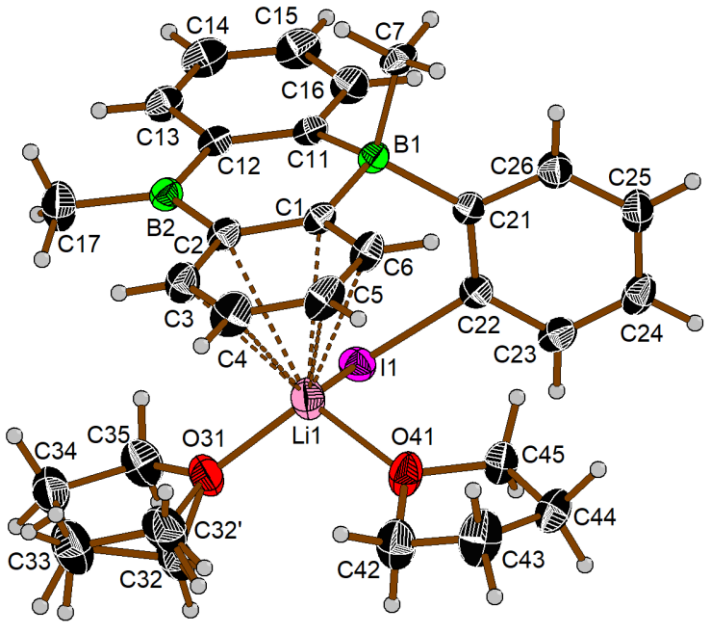

Figure S59. Molecular structure of [Li(thf)$_2$][**4**] in the solid state; atomic displacement ellipsoids are drawn at the 50% probability level.

4.3 Single-Crystal X-ray Analysis of [K(dme)][K(dme)$_2$][6]

Compound [K(dme)][K(dme)$_2$][**6**] crystallizes in the orthorhombic space group $P2_12_12_1$ (No. 19; Figure S60). Two crystallographically unique K^+ cations coordinate the anion with weak K···π(C_6) interactions (K···C distances: 3.097(2) – 3.305(2) Å). Their coordination spheres are completed by dme ligands. The whole crystal packing is chiral and the value of the Flack parameter close to zero confirms that the crystal used for the structure determination is homochiral.

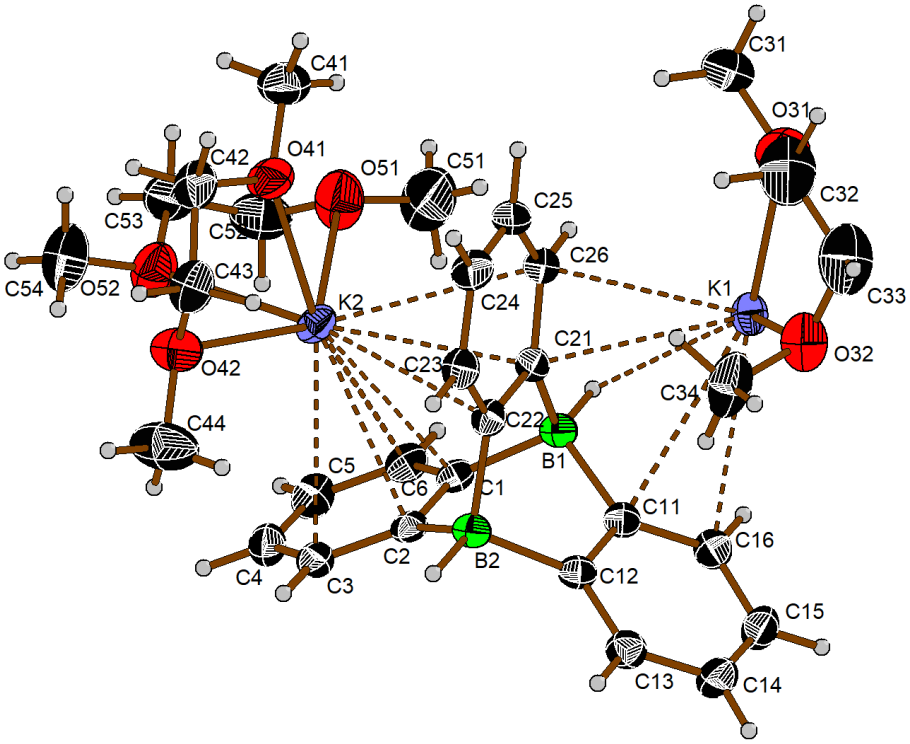

Figure S60. Molecular structure of [K(dme)][K(dme)$_2$][**6**] in the solid state; atomic displacement ellipsoids are drawn at the 50% probability level.

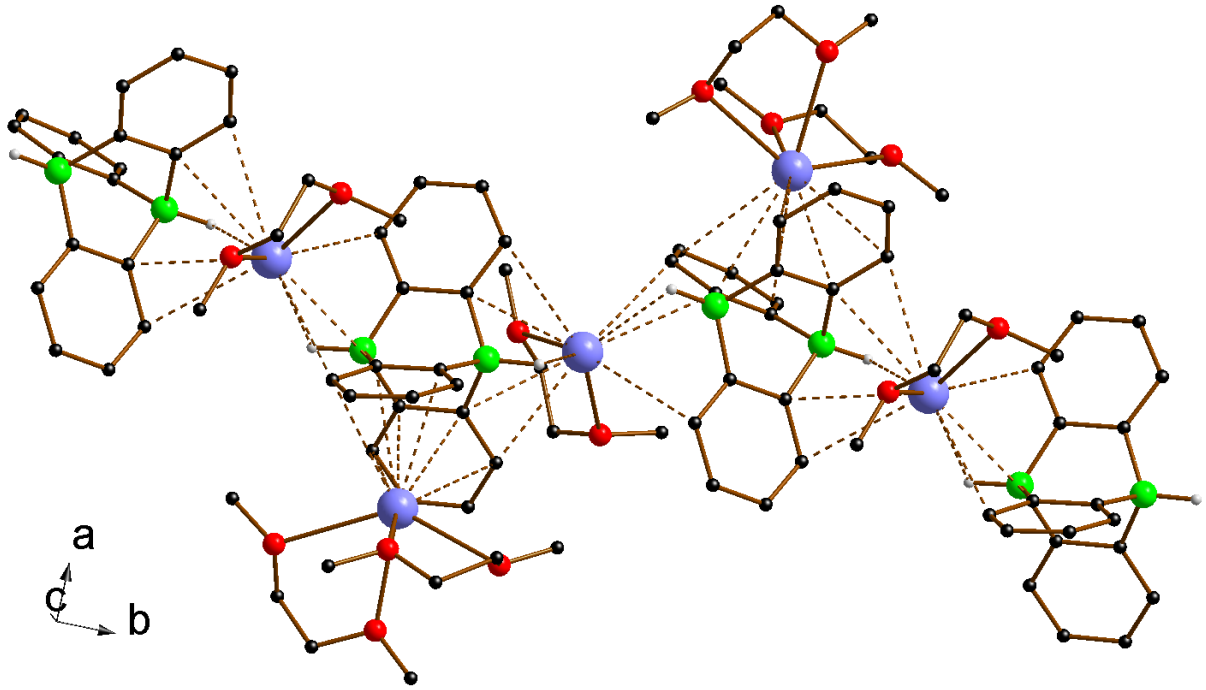

Figure S61. Coordination polymer formed by $[K(dme)]^+$ and $\{[K(dme)_2][\mathbf{6}]\}^-$ ions in the crystal lattice of $[K(dme)][K(dme)_2][\mathbf{6}]$. C-bonded H atoms are omitted for clarity.

4.4 Single-Crystal X-ray Analysis of [K(dme)][K(dme)$_2$][7]

Compound [K(dme)][K(dme)$_2$][**7**] crystallizes in the monoclinic space group $P2_1/n$ (No. 14; (a) in Figure S62). Two crystallographically unique K^+ cations coordinate the anion with weak K···π(C_6) interactions (K···C distances: 3.108(2) – 3.211(2) Å). Their coordination spheres are completed by dme ligands ((b) in Figure S62).

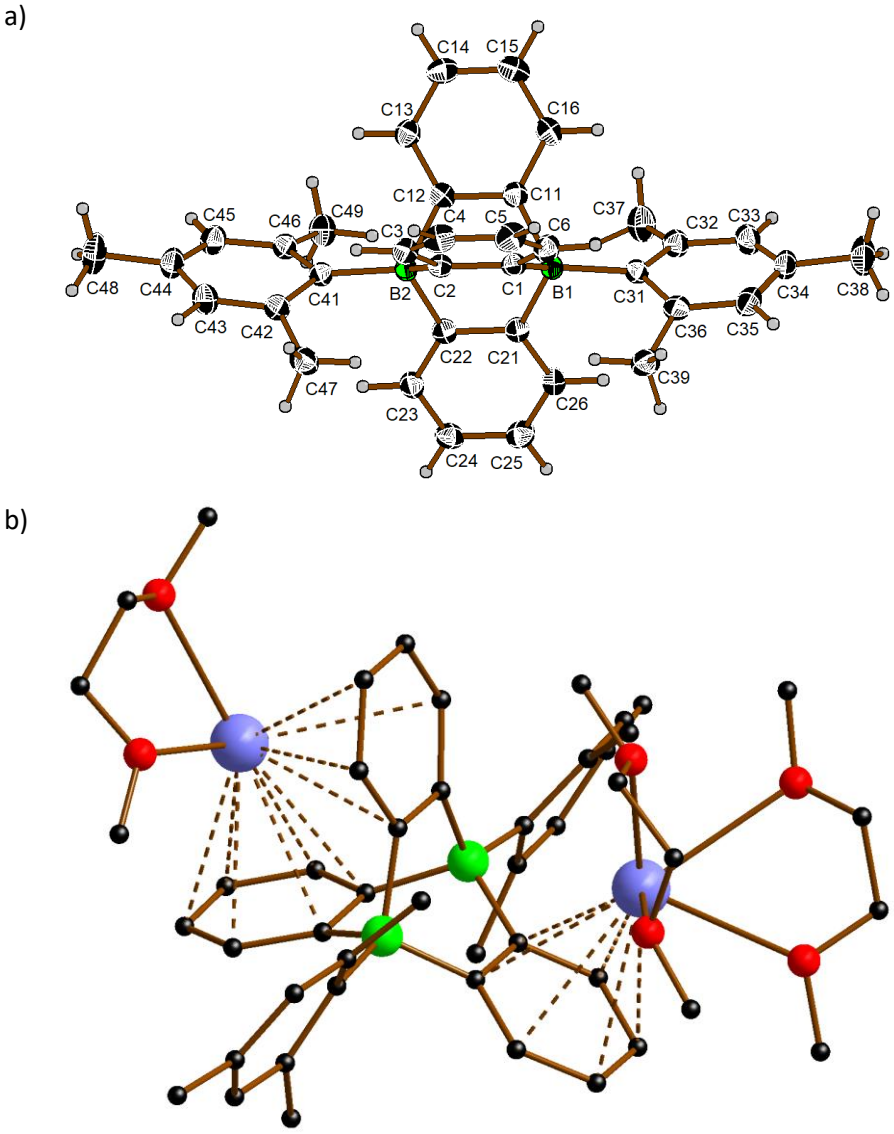

Figure S62. a) Molecular structure of the anion [**7**]$^{2-}$ in the solid state; atomic displacement ellipsoids are drawn at the 50% probability level. b) Coordination of K^+ cations (light blue spheres) in [K(dme)][K(dme)$_2$][**7**]; H atoms are omitted for clarity.

4.5 Single-Crystal X-ray Analysis of 9·CH_2Cl_2

Compound **9**·CH_2Cl_2 crystallizes in the monoclinic space group $P2_1/n$ (No. 14; Figure S63) with one solvent molecule (CH_2Cl_2) per formula unit, which is disordered over two positions.

The crystal structure demonstrates a weak sub-structural motif corresponding to the B-centering of the monoclinic cell. However, the analysis of the reflection intensities reveals that the *hkl*, *h*+*l* = 2n+1 reflections are only slightly weaker (average I_{hkl}/σ = 4.0) than in average (5.0 for all reflections). Because the tentative 'sub-structural' model (in two times smaller unit cell) demonstrates significant disorder accompanied with poor residuals' values, it seems that we observe consequences of the temperature-driven crystallographic ordering accompanied by decreasing of translational symmetry.

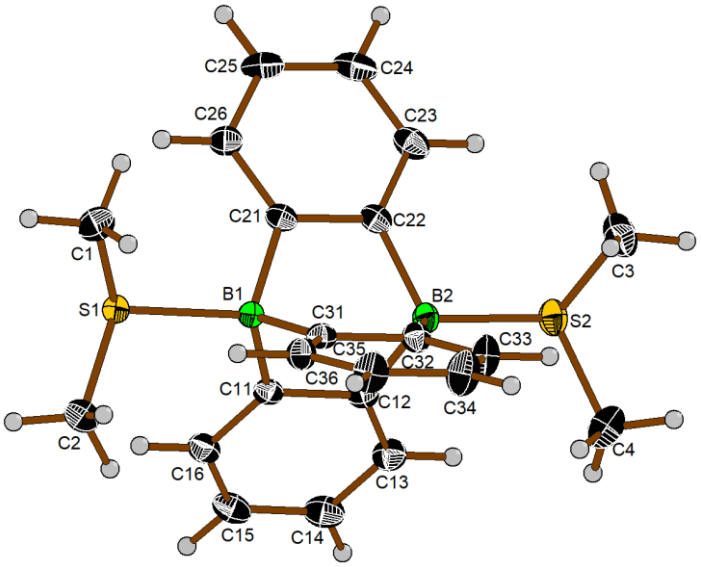

Figure S63. Molecular structure of **9**·CH_2Cl_2 in the solid state; atomic displacement ellipsoids are drawn at the 50% probability level. The solvent molecule (CH_2Cl_2) is omitted for clarity.

5. References

S1 G. R. Fulmer, A. J. M. Miller, N. H. Sherden, H. E. Gottlieb, A. Nudelman, B. M. Stoltz, J. E. Bercaw and K. I. Goldberg, *Organometallics*, 2010, **29**, 2176–2179.

S2 E. von Grotthuss, M. Diefenbach, M. Bolte, H.-W. Lerner, M. C. Holthausen and M. Wagner, *Angew. Chem. Int. Ed.*, 2016, **55**, 14067–14071.

S3 E. von Grotthuss, S. E. Prey, M. Bolte, H.-W. Lerner and M. Wagner, *J. Am. Chem. Soc.*, 2019, **141**, 6082–6091.

S4 M. Bamberg, M. Bursch, A. Hansen, M. Brandl, G. Sentis, L. Kunze, M. Bolte, H.-W. Lerner, S. Grimme and M. Wagner, *J. Am. Chem. Soc.*, 2021, **143**, 10865–10871.

S5 E. J. Lawrence, V. S. Oganesyan, D. L. Hughes, A. E. Ashley and G. G. Wildgoose, *J. Am. Chem. Soc.*, 2014, **136**, 6031–6036.

S6 N. J. Turro, M. Tobin, L. Friedman and J. B. Hamilton, *J. Am. Chem. Soc.*, 1969, **91**, 516–516.

S7 J.-D. Chai and M. Head-Gordon, *Phys. Chem. Chem. Phys.*, 2008, **10**, 6615–6620.

S8 R. Krishnan, J. S. Binkley, R. Seeger and J. A. Pople, *J. Chem. Phys.*, 1980, **72**, 650–654.

S9 A. V. Marenich, C. J. Cramer and D. G. Truhlar, *J. Phys. Chem. B*, 2009, **113**, 6378–6396.

S10 R. Ditchfield, *Mol. Phys.*, 1974, **27**, 789–807.

S11 K. Wolinski, J. F. Hinton and P. Pulay, *J. Am. Chem. Soc.*, 1990, **112**, 8251–8260.

S12 J. P. Perdew, K. Burke and M. Ernzerhof, *Phys. Rev. Lett.*, 1996, **77**, 3865–3868.

S13 S. Grimme, J. Antony, S. Ehrlich and H. Krieg, *J. Chem. Phys.*, 2010, **132**, 154104.

S14 S. Grimme, S. Ehrlich and L. Goerigk, *J. Comput. Chem.*, 2011, **32**, 1456–1465.

S15 F. Weigend and R. Ahlrichs, *Phys. Chem. Chem. Phys.*, 2005, **7**, 3297–3305.

S16 M. Henkelmann, A. Omlor, M. Bolte, V. Schünemann, H.-W. Lerner, J. Noga, P. Hrobárik and M. Wagner, *Chem. Sci.*, 2022, **13**, 1608–1617.

S17 C. Adamo and V. Barone, *Chem. Phys. Lett.*, 1998, **298**, 113–119.

S18 D. Rappoport and F. Furche, *J. Chem. Phys.*, 2010, **133**, 134105; the basis set was delivered from: K. L. Schuchardt, B. T. Didier, T. Elsethagen, L. Sun, V. Gurumoorthi, J. Chase, J. Li and T. L. Windus, *J. Chem. Inf. Model.*, 2007, **47**, 1045–1052.

S19 (*a*) A. Klamt and G. Schüürmann, *J. Chem. Soc., Perkin Trans. 2*, 1993, 799–805; (*b*) V. Barone and M. Cossi, *J. Phys. Chem. A*, 1998, **102**, 1995–2001.

S20 M. J. Frisch, G. W. Trucks, H. B. Schlegel, G. E. Scuseria, M. A. Robb, J. R. Cheeseman, G. Scalmani, V. Barone, G. A. Petersson, H. Nakatsuji, X. Li, M. Caricato, A. V. Marenich, J. Blonio, B. G. Janesko, R. Gomperts, B. Mennucci, H. P. Hratchian, J. V. Ortiz, A. F. Izmaylov, J. L. Sonnenberg, D. Williams-Young, F. Ding, F. Lipparini, F. Egidi, J. Goings, B. Peng, A. Petrone, T. Henderson, D. Ranasinghe, V. G. Zakrzewski, J. Gao, N. Rega, G. Zheng, W. Liang, M. Hada, M. Ehara, K. Toyota, R. Fukuda, J. Hasegawa, M. Ishida, T. Nakajima, Y. Honda, O. Kitao, H. Nakai, T. Vreven, K. Throssell, J. A. Montgomery Jr., J. E. Peralta, F. Ogliaro, M. J. Bearpark, J. J. Heyd, E. N. Brothers, K. N. Kudin, V. N. Staroverov, T. A. Keith, R. Kobayashi, J. Normand, K. Raghavachari, A. P. Rendell, J. C. Burant, S. S. Iyengar, J. Tomasi, M. Cossi, J. M. Millam, M. Klene, C. Adamo, R. Cammi, J. W. Ochterski, R. L. Martin, K. Morokuma, O. Farkas, J. B. Foresman and D. J. Fox, *Gaussian 09, Revision D.01*, 2016.

S21 M. J. Frisch, G. W. Trucks, H. B. Schlegel, G. E. Scuseria, M. A. Robb, J. R. Cheeseman, G. Scalmani, V. Barone, G. A. Peterson, H. Nakatsuji, X. Li, M. Caricato, A. V. Marenich, J. Bloino, B. G. Janesko, R. Gomperts, B. Mennucci, H. P. Hratchian, J. V. Ortiz, A. F. Izmaylov, J. L. Sonnenberg, D. Williams-Young, F. Ding, F. Lipparini, F. Egidi, J. Goings, B. Peng, A. Petrone, T. Henderson, D. Ranasinghe, V. G. Zakrzewski, J. Gao, N. Rega, G. Zheng, W. Liang, M. Hada, M. Ehara, K. Toyota, R. Fukuda, J. Hasegawa, M. Ishida, T. Nakajima, Y. Honda, O. Kitao, H. Nakai, T. Vreven, K. Throssell, J. A. Montgomery Jr., J. E. Peralta, F. Ogliaro, M. J. Bearpark, J. J. Heyd, E. N. Brothers, K. N. Kudin, V. N. Staroverov, T. A. Keith, R. Kobayashi, J. Normand, K. Raghavachari, A. P. Rendell, J. C. Burant, S. S. Iyengar, J. Tomasi, M. Cossi, J. M. Millam, M. Klene, C. Adamo, R. Cammi, J. W. Ochterski, R. L. Martin, K. Morokuma, O. Farkas, J. B. Foresman and D. J. Fox, *Gaussian 16, Revision B.01*, 2016.

S22 (*a*) F. Neese, *WIREs Comput. Mol. Sci.*, 2012, **2**, 73–78; (*b*) F. Neese, WIREs *Comput. Mol. Sci.*, 2022, **12**, e1606.

S23 C. Y. Legault, *CYLview, 1.0b*, 2009.

S24 (*a*) C. Riplinger and F. Neese, *J. Chem. Phys.*, 2013, **138**, 034106; (*b*) Y. Guo, C. Riplinger, U. Becker, D. G. Liakos, Y. Minenkov, L. Cavallo and F. Neese, *J. Chem. Phys.*, 2018, **148**, 011101.

S25 G. M. Sheldrick, *SHELXS-97 and SHELXL-97, Program for Crystal Structure Solution and Refinement*, 1997.

S26 G. M. Sheldrick, *Acta Crystallogr. Sect. A Found. Adv.*, 2015, **71**, 3–8.